Advances in Differential Equations and Control Processes 2026, 33(3), 4667.
doi: https://doi.org/10.59400/adecp4667

Article

Wellbore-reservoir coupled simulation study for CO_2 flooding in oil reservoirs

Bujie Ding[1], Huanying Ma[1], Jincang Li[1], Kaifang Jin[1], Xuze Liu[1], Tao Zou[1], Hui Zhao[2,3,*], Jiaxu Liu[2,3,*], Siyuan Chen[2,3], Xi Ouyang[2,3], Xiang Rao[2,3,4,*]

[1] China Oilfield Services Limited, Sanhe 065201, China; dingbj@cosl.com.cn (BD); mahy2@cosl.com.cn (HM); lijc9@cosl.com.cn (JL); jinkf@cosl.com.cn (KJ); liuxz6@cosl.com.cn (XL); ex_zoutao2@cosl.com.cn (TZ)
[2] School of Petroleum Engineering, Yangtze University, Wuhan 430100, China; chensiyuanhai@outlook.com (SC); 2024720443@yangtzeu.edu.cn (XO)
[3] State Key Laboratory of Low-Carbon Catalysis and Carbon Dioxide Utilization, Yangtze University, Wuhan 430100, China
[4] School of Computer Science, Yangtze University, Wuhan 430100, China
*** Corresponding authors:** Hui Zhao, zhaohui@yangtzeu.edu.cn; Jiaxu Liu, liujiaxuhai@outlook.com or 2022005721@yangtzeu.edu.cn; Xiang Rao, raoxiang@yangtzeu.edu.cn

CITATION

Ding B, Ma H, Li J, et al. Wellbore-reservoir coupled simulation study for CO_2 flooding in oil reservoirs. Advances in Differential Equations and Control Processes. 2026; 33(3): 4667. https://doi.org/10.59400/adecp4667

ARTICLE INFO

Received: 13 July 2026
Revised: 15 August 2026
Accepted: 20 August 2026
Available online: 27 August 2026

Abstract: CO_2 flooding can simultaneously enhance oil recovery and enable geological carbon storage. This study develops a tNavigator-based coupled wellbore-reservoir CO_2 flooding model to examine tubing-head-to-downhole pressure conversion and early gas breakthrough through a high-permeability channel. A three-dimensional isothermal compositional model represents reservoir flow, while vertical flow performance (VFP) tables constructed using the Beggs-Brill correlation describe wellbore multiphase flow and pressure conversion. The coupled VFP relationships, well flow equations, and reservoir mass-conservation equations are solved using the adaptive implicit method (AIM) implemented in tNavigator, enabling bidirectional interactions among wellbore pressure variation, downhole boundary conditions, and reservoir dynamic parameters. A continuous high-permeability channel between injectors and producers is incorporated to characterize reservoir heterogeneity. Simulations under fixed injection rate and fixed tubing-head pressure conditions are conducted to analyze the influences of injection and production rates, porosity and streak permeability on CO_2 migration and flooding performance. The results show that injection and liquid production rates dominate the inter-well pressure difference and control gas breakthrough. Reservoir porosity primarily governs reservoir storage and pressure buffering capacity, while streak permeability determines CO_2 preferential migration velocity. Under tubing-head pressure constraints, actual injection and production performances are co-regulated by tubing-head pressure limits, wellbore pressure loss and reservoir injectivity/deliverability. The proposed model provides a numerical framework for investigating wellbore-reservoir interactions and gas-channeling risks in heterogeneous reservoirs with high-permeability channels. Quantitative validation against field measurements or controlled experimental data will be undertaken in future work.

Keywords: CO_2 flooding; wellbore-reservoir coupling; tNavigator; high-permeability channel; VFP table

1. Introduction

Driven by the growing demand for carbon emission reduction and the continued implementation of China's "dual-carbon" strategy, carbon capture, utilization, and storage (CCUS) has become a key technological pathway for the low-carbon transition of the petroleum industry. The Intergovernmental Panel on Climate Change (IPCC) [1] systematically summarized the major technical routes for CO_2 capture, transportation, and geological storage, highlighting that injecting captured CO_2 into suitable subsurface formations is an effective approach for mitigating greenhouse gas emissions. Bachu [2] further evaluated the storage mechanisms, technical requirements, and implementation challenges of CO_2 sequestration in deep saline aquifers, depleted oil and gas reservoirs, and producing reservoirs, demonstrating the substantial geological storage potential of subsurface formations. In petroleum reservoir development, Godec et al. [3] investigated the application of anthropogenic CO_2 for enhanced oil recovery (EOR) and geological storage, showing that CO_2-EOR can simultaneously increase oil production while permanently retaining a portion of the injected CO_2 underground. Núñez-López and Moskal [4] also pointed out that CO_2-EOR provides considerable engineering potential for achieving both enhanced hydrocarbon recovery and carbon emission reduction. Recent studies have shown that shale-oil adsorption and pore plugging, water-injection well patterns, pore-scale CO_2–oil miscible flow, and gas-channeling control all strongly affect fluid transport and sweep efficiency in unconventional reservoirs [5–8]. Numerical formulations for heterogeneous and fractured reservoir flow have likewise continued to develop [9, 10]. Sheng [11] demonstrated that gas injection possesses superior injectivity and diffusion capability in low-permeability formations. Song et al. [12] comprehensively reviewed CO_2-EOR applications in tight oil reservoirs in North America and China, concluding that CO_2 improves oil mobility through diffusion, dissolution, oil swelling, and viscosity reduction, making it particularly suitable for tight and highly heterogeneous reservoirs. Earlier, Holm and Josendal [13] systematically investigated the mechanisms of CO_2 flooding, including oil dissolution, swelling, viscosity reduction, and light-hydrocarbon extraction, and demonstrated that CO_2 injection can effectively improve crude-oil properties and enhance displacement efficiency. Consequently, CO_2 flooding not only provides an effective means of sustaining oil production during the late development stage of reservoirs but also offers a practical pathway for permanent geological storage of captured CO_2, thereby simultaneously improving oil recovery and contributing to carbon emission mitigation.

Considerable efforts have been devoted to understanding the mechanisms of CO_2 flooding and developing compositional reservoir simulation methods. Stalkup [14] systematically established the fundamental theory of miscible gas flooding and the associated mass-transfer mechanisms between injected gas and crude oil, demonstrating that miscible or near-miscible displacement can be achieved through multiple-contact processes under appropriate pressure and fluid-composition conditions. Orr [15] further elucidated the formation mechanisms of miscibility during gas injection from the perspectives of phase behavior and multicomponent mass transfer. Kumar et al. [16] comprehensively reviewed the fundamental mechanisms and recent advances in CO_2 miscible flooding for enhanced oil recovery, concluding that CO_2 improves displacement efficiency by promoting oil swelling, reducing oil viscosity and interfacial tension, and extracting light hydrocarbons. Recent studies have further clarified the multiscale mechanisms controlling CO_2 displacement in low-permeability reservoirs. Wang et al. [17] analyzed the sensitivity of CO_2 miscible flooding to oil viscosity, permeability, permeability contrast, and pressure, and identified the dominant recovery mechanisms under different reservoir conditions. Ren et al. [18] combined nuclear magnetic resonance experiments with the volume-of-fluid method to compare miscible and immiscible CO_2 flooding, revealing distinct pore-scale displacement patterns and viscous fingering behavior. Song et al. [19] employed a phase-field model to investigate the effects of key pore-scale parameters on CO_2–oil two-phase flow and displacement efficiency. Chi et al. [20] developed a numerical model for CO_2 immiscible flooding in ultra-low-permeability reservoirs by incorporating crude-oil viscosity variation and the starting pressure gradient. These studies provide a multiscale basis for interpreting CO_2 transport, phase redistribution, and displacement behavior in heterogeneous reservoirs. Owing to the complex multiphase flow and phase behavior involving CO_2 and hydrocarbon components during the flooding process, compositional reservoir simulation has become an essential tool for accurately describing component transport and phase transitions [21, 22]. The Peng-Robinson equation of state proposed by Peng and Robinson [23] provides the theoretical foundation for predicting phase equilibrium, fluid density, and thermophysical properties of CO_2–hydrocarbon systems. Based on the equation-of-state formulation, Coats [24] developed a compositional reservoir simulation model capable of describing component partitioning and phase behavior in oil–gas systems. Nghiem et al. [25] further extended equation-of-state compositional simulation to model phase equilibrium and dynamic reservoir responses in multicomponent systems. Young and Stephenson [26] subsequently proposed a generalized compositional reservoir simulation framework, providing a numerical basis for predicting component transport, pressure propagation, and gas breakthrough during complex gas-injection processes.

Wellbore multiphase flow and wellbore-reservoir coupling have also received considerable attention in CO_2 flooding studies, as tubing-head pressure conditions must be translated into the actual bottom-hole injection and production boundaries through wellbore flow. Beggs and Brill [27] developed the classical multiphase flow correlation based on gas–liquid flow experiments in inclined pipes, in which flow pattern, liquid holdup, gravitational pressure loss, and frictional pressure loss are comprehensively considered. Hasan et al. [28] developed an integrated wellbore-reservoir simulation approach and demonstrated that wellbore pressure losses modify the bottom-hole flowing pressure, thereby influencing reservoir production performance. Da Silva and Jansen [29] reviewed dynamic wellbore-reservoir coupling methods and pointed out that the pressure and flow-rate interactions between the wellbore and the reservoir constitute a critical component of production forecasting for complex oil and gas reservoirs. Peng et al. [30] further summarized recent developments in dynamic wellbore-reservoir coupling under two-phase flow conditions and concluded that coupled simulation improves the prediction accuracy of bottom-hole pressure, well flow rate, and reservoir dynamic behavior. Focusing on CO_2 injection, Abdelaal and Zeidouni [31] established a coupled wellbore-reservoir model for multilayer geological storage formations to evaluate the effects of wellbore pressure losses and formation-property variations on the distribution of CO_2 injection among different layers. Zamani et al. [32] developed a coupled wellbore-aquifer model that simultaneously describes pressure evolution, temperature variation, and near-wellbore dry-out during CO_2 injection, demonstrating the importance of consistent information exchange between the wellbore and the formation. Tavagh Mohammadi et al. [33] systematically reviewed transient wellbore-reservoir coupling approaches for CO_2 injection and emphasized that wellbore dynamics and reservoir injectivity should be evaluated within an integrated simulation framework. Although these studies mainly focus on geological storage formations, their coupling principles are directly relevant to the conversion of tubing-head pressure constraints into dynamic bottom-hole boundary conditions in CO_2 flooding simulations.

Reservoir heterogeneity is another key factor affecting CO_2 migration and gas breakthrough during CO_2 flooding. Koval [34] demonstrated that mobility contrast and reservoir heterogeneity promote viscous fingering and non-uniform displacement during unstable miscible flooding in heterogeneous porous media. Luo et al. [35] investigated the influence of reservoir heterogeneity on CO_2 flooding performance in tight oil reservoirs and reported that permeability variations significantly alter the morphology of the CO_2 displacement front, sweep efficiency, and breakthrough time. Khan and Mandal [36] analyzed the effects of permeability contrast on water-alternating-gas (WAG) flooding in highly stratified heterogeneous reservoirs and found that high-permeability zones readily develop preferential flow channels, thereby accelerating gas migration toward production wells while reducing sweep efficiency in low-permeability regions. Li et al. [37] established a mathematical model to characterize the CO_2 front and miscible-zone front and to quantitatively identify the onset of gas channeling, providing a basis for evaluating CO_2 breakthrough in low-permeability reservoirs. Zhang et al. [38] combined laboratory experiments with numerical simulation to optimize balanced CO_2 displacement in a multilayer low-permeability reservoir, showing that coordinated injection and production can delay gas channeling and improve interlayer displacement uniformity. Li et al. [39] investigated the Daqingzijing Block in the Jilin Oilfield and demonstrated that the non-uniform distribution of permeability significantly affects CO_2 migration, oil recovery, and storage performance. Zhang et al. [40] systematically reviewed CO_2 front propagation and sweep characteristics and identified premature fingering and gas channeling as major limitations on sweep efficiency. These findings further support the introduction of a continuous high-permeability channel in the present model to investigate preferential CO_2 migration, non-uniform displacement, and early gas breakthrough.

In summary, substantial progress has been made in understanding the mechanisms of CO_2 flooding, compositional reservoir simulation, wellbore multiphase flow, wellbore-reservoir coupling, and the effects of reservoir heterogeneity. However, for compositional multiphase CO_2 flooding in reservoirs containing high-permeability channels, the coupled interactions among tubing-head pressure constraints, wellbore pressure losses, dynamic bottom-hole boundary conditions, and CO_2 migration within the reservoir have not yet been fully understood. To address this issue, this study develops a coupled wellbore-reservoir simulation model for CO_2 flooding using the tNavigator platform. A continuous high-permeability channel is introduced along the line connecting the injection and production wells, and coupled simulations are conducted under both fixed-rate and fixed tubing-head-pressure operating conditions. Furthermore, sensitivity analyses are performed on the CO_2 injection rate, liquid production rate, reservoir porosity, and streak permeability to investigate their effects on bottom-hole flowing pressure, CO_2-front propagation, gas breakthrough, and gas channeling behavior. The proposed model provides a numerical basis for optimizing injection–production strategies and evaluating reservoir performance and gas-channeling risks in reservoirs containing high-permeability channels. The present study is designed as a mechanistic numerical investigation rather than a field-history-matched case study. Accordingly, its primary objective is to identify wellbore-reservoir coupled response mechanisms and parameter sensitivities under controlled numerical conditions. Quantitative validation using measured tubing-head and bottom-hole pressures, injection and production histories, fluid-composition data, and gas-breakthrough information will be conducted in future work.

2. Mathematical model and simulation methods

This section presents the theoretical formulation and numerical implementation of the coupled wellbore-reservoir model for CO_2 flooding. First, the governing equations and phase-behavior constraints for compositional multiphase flow in the reservoir are established. The governing equations are then discretized using the finite volume method. Subsequently, the coupling relationship between wellbore flow and reservoir flow is formulated. Finally, the implementation procedure of the proposed model in the tNavigator simulator is described.

2.1. CO_2 flooding reservoir mathematical model based on tNavigator

Under isothermal compositional multiphase flow conditions, the molar conservation equation for each component i in porous media can be written as:

$$\frac{\partial}{\partial t}\left(\phi N_i\right) + \nabla \cdot \sum_{\alpha=O,W,G} x_{i\alpha}\xi_\alpha \boldsymbol{u_\alpha} = q_i,\ i = 1, 2, \ldots, N_c \tag{1}$$

where ϕ is the porosity, N_i is the total molar density of component i, α denotes the oil, water, and gas phases, $x_{i\alpha}$ is the mole fraction of component i in phase α, ξ_α is the molar density of phase α, $\boldsymbol{u_\alpha}$ is the phase velocity, q_i is the source/sink term of component i, and N_c is the total number of components. The flow of each phase is governed by Darcy's law:

$$\boldsymbol{u_\alpha} = -\mathrm{K}\frac{k_{r\alpha}}{\mu_\alpha}\left(\nabla p_\alpha - \rho_\alpha g \nabla D\right) \tag{2}$$

where K is the absolute permeability tensor, $k_{r\alpha}$ is the relative permeability, μ_α is the phase viscosity, p_α is the phase pressure, p_α is the phase density, g is the gravitational acceleration, and D is the depth.

The Peng–Robinson (PR) equation of state (EOS) is employed to describe the phase behavior of the CO_2–hydrocarbon system. The PR EOS is a cubic equation of state and is expressed as:

$$p = \frac{RT}{v-b} - \frac{a}{v^2 + 2bv - b^2} \tag{3}$$

where R is the universal gas constant, T is the absolute temperature, v is the molar volume, a and b are the mixture parameters, and Ω_{a0} and Ω_{b0} are the constants of the Peng–Robinson equation of state. For multicomponent systems, the mixture parameters a and b are calculated from the component mole fractions and binary interaction coefficients. In the PR equation of state, $\Omega_{a0} = 0.457235529$ and $\Omega_{b0} = 0.077796074$. The PR equation of state is used to calculate the phase equilibrium, phase densities, and fluid properties of the CO_2–crude oil system under different pressure and compositional conditions. In addition, the model satisfies the capillary-pressure relationships and saturation constraints:

$$P_{c,GO} = p_g - p_o,\ P_{c,OW} = p_o - p_w, S_o + S_w + S_g = 1, \tag{4}$$

where S_O, S_W, and S_G denote the oil-, water-, and gas-phase saturations, respectively; and $P_{c,GO}$ and $P_{c,OW}$ represent the gas–oil and oil–water capillary pressures, respectively.

2.2. Finite volume spatial discretization of governing equations

According to the tNavigator User Manual, the simulator employs the finite volume method (FVM) on a block-centered grid for spatial discretization, while the coefficients associated with phase saturation are evaluated using the standard upstream weighting scheme. Following this discretization procedure, the component conservation equation given by Equation (1) is integrated over grid cell m, and the divergence term is transformed into the summation of component fluxes across all cell faces, yielding:

$$\frac{d}{dt}\left[V_m\left(\phi N_i\right)_m\right] + \sum_{f\in\partial\Omega_m}\sum_{\alpha=O,W,G} A_f\left(x_{i\alpha}\xi_\alpha \boldsymbol{u}_\alpha\right)_f \cdot \boldsymbol{n}_f = V_m q_{i,m} \tag{5}$$

where Ω_m is the m-th control volume, $V_m = |\Omega_m|$ is its volume, $f \in \partial\Omega_m$ denotes a cell face of the control volume, A_f and $\boldsymbol{n}_f$ are the face area and the outward unit normal vector, respectively, and $q_{i,m}$ is the average source/sink term of component i within grid cell. The resulting semi-discrete equations are advanced in time and solved together with the equation of state, the capillary-pressure relationships, and the saturation constraints, leading to a nonlinear system of equations at each time step:

$$\boldsymbol{F}\left(p, N_1, \ldots, N_{N_c}\right) = 0 \tag{6}$$

2.3. Wellbore-reservoir coupling

At each time step, the coupled VFP relationships, well connection flow equations, and reservoir component-conservation equations were solved using the adaptive implicit method implemented in tNavigator. The default convergence and iteration-control settings of tNavigator 25.1, as summarized in **Table 1**, were adopted. A time step was accepted when the nonlinear convergence and component material-balance criteria were satisfied within the prescribed iteration limits. If these criteria were not satisfied or the Newton convergence rate became too low, the current step was rejected and recalculated using an automatically reduced time step.

Table 1. Convergence and iteration-control parameters for the coupled wellbore–reservoir solution.

Parameter	Definition	Value
TOLNEWT	Convergence tolerance for the nonlinear residual norm	1.0×10^{-3}
TOLVARNEWT	Convergence tolerance for the maximum variation of primary variables	1.0×10^{-3}
MBERRCTRL	Control tolerance for the component material-balance error	1.0×10^{-5}
MAXNEWTIT	Maximum number of Newton iterations per time step	100
MAXWELLIT	Maximum number of well iterations per well	8
THPWELLPARAMTOL	Convergence tolerance for converting tubing-head pressure to bottom-hole flowing pressure	1.0×10^{-3}
Initial internal time step	Initial internal time-step size used by the simulator	0.1 d
Minimum internal time step	Minimum allowable internal time-step size	0.001 d

On the wellbore side, the Beggs-Brill multiphase flow correlation is employed to calculate the gravitational, frictional, and acceleration pressure losses. The relationships among the tubing-head pressure, bottom-hole flowing pressure, well flow rate, and wellstream properties are represented using vertical flow performance (VFP) tables. The wellbore and reservoir models are coupled through the bottom-hole flowing pressure and well source/sink terms. For a given bottom-hole flowing pressure, the reservoir model calculates the phase flow rates and component flow rates in each perforated grid cell using the well connection flow equation, after which the wellbore model updates the wellbore pressure losses and bottom-hole flowing pressure according to the well flow rate and fluid composition.

2.4. Simulation implementation workflow

Three simulation cases were established based on the tNavigator numerical simulation platform. The implementation workflow consisted of geological model construction, fluid and rock property definition, development strategy specification, coupled simulation, and result analysis. First, a three-dimensional Cartesian grid model was constructed, and the effective reservoir intervals were defined to provide the spatial discretization framework for subsequent flow simulations. Reservoir properties, including porosity, permeability, initial pressure, and initial oil saturation, were then assigned to each reservoir layer. In the fluid model, CO_2 and hydrocarbon components were defined as the primary components of the compositional model. The Peng-Robinson equation of state was employed to describe fluid phase behavior, while the Lohrenz-Bray-Clark viscosity correlation was used to calculate fluid viscosity. Subsequently, oil–water and gas–oil relative permeability curves were incorporated to characterize the flow behavior of each fluid phase in porous media during CO_2 injection. Subsequently, the injection and production wells were incorporated into the model, and their perforated intervals were specified. Separate VFP tables were constructed for the injection and production wells according to the corresponding wellstream fluids.

Finally, the well operating-control modes were specified, and the coupled simulation was performed.

To evaluate CO_2 storage performance, the cumulative stored amount of CO_2 was calculated from the difference between cumulative CO_2 injection and cumulative CO_2 production:

$$M_{sto} = M_{inj} - M_{prod} \tag{7}$$

The CO_2 storage efficiency was defined as:

$$\eta_{sto} = \frac{M_{sto}}{M_{inj}} \times 100\%$$

Where M_{inj}, M_{prod}, and M_{sto} denote the cumulative injected, produced, and stored amounts of CO_2, respectively.

3. Case 1: Establishment and design of the base model

3.1. Reservoir model

A three-dimensional Cartesian grid was adopted to represent the reservoir domain in this case. The reservoir model has dimensions of 200 m × 200 m × 20 m, with a grid spacing of 10 m in both horizontal directions. Vertically, the reservoir is divided into three layers: Layer 1 extends from 1,000 m to 1,010 m, Layer 2 from 1,010 m to 1,015 m, and Layer 3 from 1,015 m to 1,020 m. The total simulation period is 1,880 days, which is divided into 188 time steps with an interval of 10 days. An injection well is located at (5, 5), and a production well is located at (195, 195). Both wells are vertical wells operated under fixed-rate control. The injection well is assigned a constant CO_2 injection rate of 5,000 sm^3/day using pure CO_2, while the production well is operated at a constant liquid production rate of 30 sm^3/day. Isotropic permeability is assumed at the grid scale, with each grid block satisfying $K_x = K_y = K_z$. However, the reservoir exhibits spatially heterogeneous permeability, with different permeability values assigned to different layers. In addition, a high-permeability channel penetrating all three layers is introduced between the injection and production wells. The permeability of the grid blocks within the channel is ten times that of the surrounding reservoir. The channel was introduced as an idealized representation of a vertically connected preferential-flow pathway, which may be associated with fracture corridors, connected channelized sand bodies, or preferential pathways enhanced by previous water flooding. Its straight geometry and continuity across all three layers do not represent a specific field-scale geological body, but were adopted to isolate the influence of channel connectivity and permeability on the wellbore-reservoir response. Consequently, the model may overestimate interlayer connectivity, directional CO_2 migration, and the severity of gas channeling. The corresponding results should therefore be interpreted as an upper-bound assessment of the effects of a highly connected preferential-flow pathway. The reservoir grid model and the high-permeability channel are illustrated in **Figure 1**, and the key parameters of this case are summarized in **Table 2**.

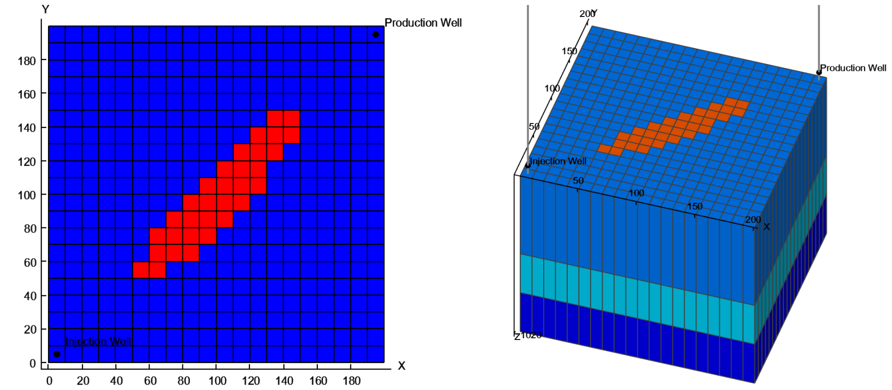

(a) 2D grid model view of case 1.

(b) 3D grid model view of case 1.

Figure 1. Geological model view of case 1.

Table 2. Core reservoir and wellbore parameters of case 1.

Parameter	Value	Parameter	Value
Layer 1 permeability	50 mD	Layer 1 porosity	0.18
Layer 2 permeability	65 mD	Layer 2 porosity	0.20
Layer 3 permeability	35 mD	Layer 3 porosity	0.22
Rock compressibility	1×10^{-6} bar^{-1}	Reference pressure	150 bar
Tubing inner diameter	0.062 m	Skin factor	2
Wellbore temperature	100 °C	Reservoir temperature	100 °C
Initial pressure	170 bar	Initial water saturation	0.20

3.2. Fluid model

A pseudo-component approach was adopted to construct the fluid compositional model. **Table 3** presents the pseudo-component classification and the initial molar composition of the reservoir fluid. The compositional system and the initial fluid composition were used as the unified fluid model for all simulation cases. In the sensitivity analyses, only the corresponding engineering or reservoir parameters were varied, whereas the initial reservoir fluid composition remained unchanged. The initial reservoir CO_2 mole fraction was 0, whereas the injected gas was pure CO_2 with a CO_2 mole fraction of 1. **Figure 2** shows the relative permeability curves adopted in this study. The connate-water saturation indicated by the relative permeability curves is 0.20, consistent with the initial water saturation specified in **Table 2**.

Table 3. Component classification and initial molar composition of reservoir fluids in each case.

Component	Mole fraction ($\sum = 1$)
CO_2	0
C_1	0.05
C_2–C_5	0.1
C_6–C_{10}	0.3
C_{11}–C_{15}	0.35
$C_{16}+$	0.2

As shown in **Table 4**, the critical properties of the pseudo-components adopted in the compositional model include molecular weight, critical temperature, critical pressure, acentric factor, and critical molar volume.

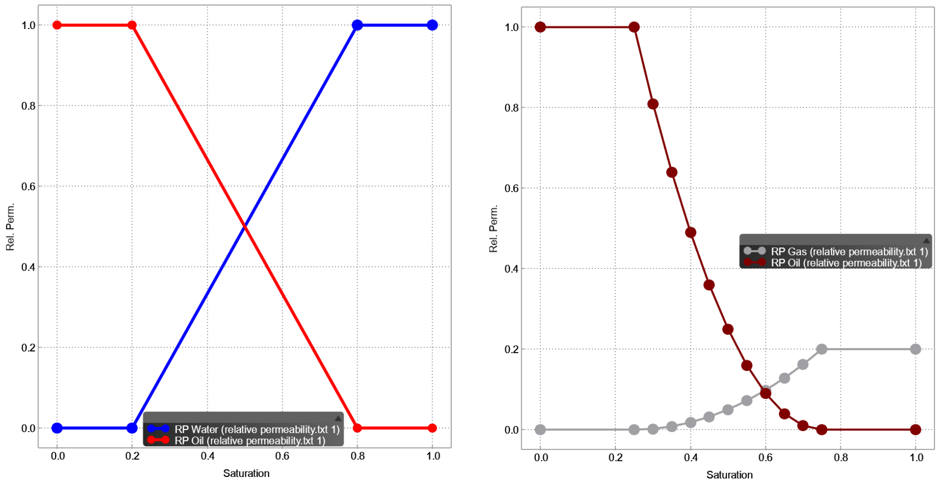

(a) Oil–water relative permeability curves. **(b)** Oil–gas relative permeability curves.

Figure 2. Fluid relative permeability curves.

Table 4. Critical properties of the pseudo-components.

Component	Molecular weight (kg/kmol)	Critical temperature (K)	Critical pressure (bar)	Acentric factor	Critical molar volume (m^3/kmol)
CO_2	44.01	304.2	73.8	0.225	0.094
C_1	16.04	190.6	46	0.012	0.099
C_2–C_5	50	380	38	0.15	0.2
C_6–C_{10}	110	550	30	0.3	0.4
C_{11}–C_{15}	180	680	20	0.5	0.65
$C_{16}+$	300	800	12	0.8	1.1

The binary interaction coefficients among the pseudo-components used in the Peng–Robinson equation-of-state calculations are listed in **Table 5**. The binary interaction coefficient matrix is symmetric, and all diagonal entries are zero.

Table 5. Binary interaction coefficients of the pseudo-components.

Component	CO_2	C_1	C_2–C_5	C_6–C_{10}	C_{11}–C_{15}	$C_{16}+$
CO_2	0	0.105	0.13	0.115	0.115	0.115
C_1	0.105	0	0	0.03	0.04	0.05
C_2–C_5	0.13	0	0	0	0	0
C_6–C_{10}	0.115	0.03	0	0	0	0
C_{11}–C_{15}	0.115	0.04	0	0	0	0
$C_{16}+$	0.115	0.05	0	0	0	0

3.3. Wellbore model

The perforated interval of the injection well extends from 1,015 m to 1,020 m, whereas the production well is perforated over the interval from 1,000 m to 1,020 m. **Figure 3** illustrates the wellbore configuration of the production well. Separate VFP tables were constructed for the injection and production wells at a reference vertical depth of 1,000 m. As shown in **Figure 4**, the injection-well VFP table uses tubing-head pressure (THP) and gas injection rate (FLO) as independent variables, with ranges of 3.7–400 bar and 100–60,000 sm^3/day, respectively. The production-well VFP table uses THP, liquid production rate (FLO), water cut (WCT), and gas–oil ratio (GOR) as independent variables, with ranges of 4–500 bar, 0.4–500 sm^3/day, 0–0.8, and 0–5,000 sm^3/sm^3, respectively.

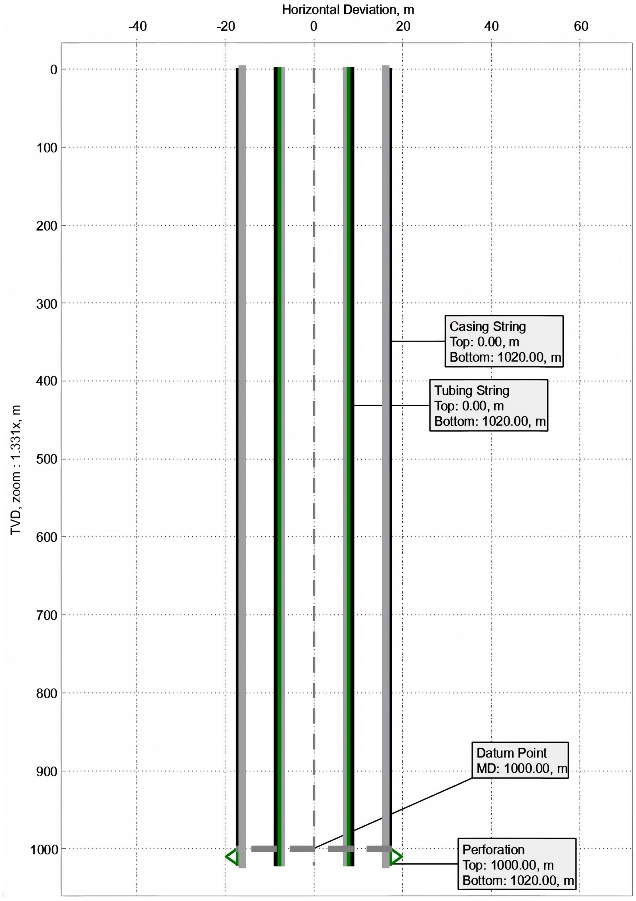

Figure 3. Wellbore structure model of the production well in Case 1.

The default tNavigator settings, VFPTABL = 1 and WVFPEXP = IMP, were adopted. Accordingly, bottom-hole flowing pressure was calculated by linear interpolation along each active VFP-table dimension. For the injection well, interpolation was performed with respect to gas injection rate and tubing-head pressure. For the production well, interpolation was performed with respect to liquid production rate, tubing-head pressure, water cut, and gas–oil ratio, using the latest water-cut and gas–oil-ratio values from the current nonlinear iteration. The artificial-lift variable was fixed at zero and therefore did not constitute an active interpolation dimension.

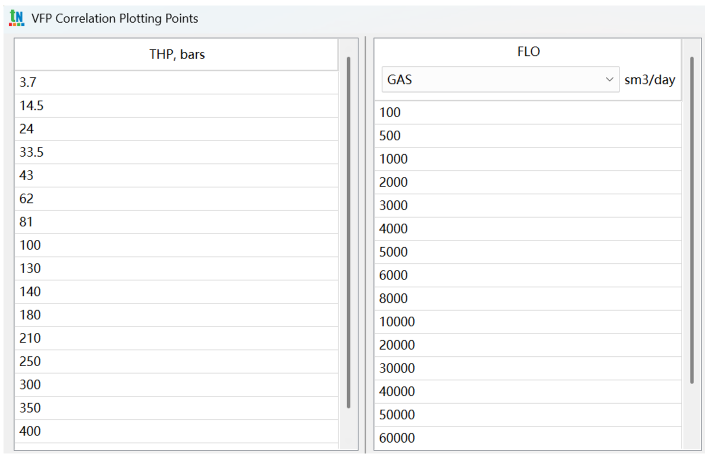

(a) Injection well.

Figure 4. *Cont.*

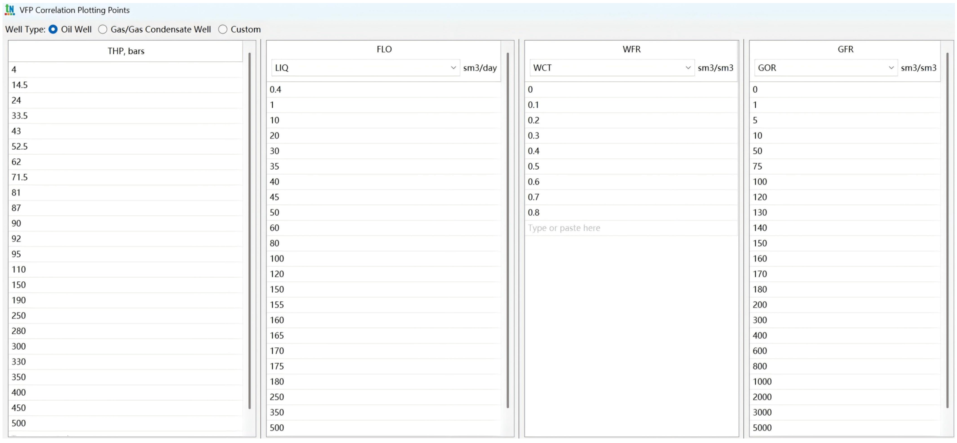

(b) Production well.

Figure 4. Sampling points used to construct the VFP tables.

4. Case 2: Sensitivity analysis of key parameters

Based on Case 1, a sensitivity analysis was conducted on four parameters, namely the CO_2 injection rate, liquid production rate, reservoir porosity, and streak permeability. The sensitivity analysis schemes considered in Case 2 are summarized in **Table 6**.

Table 6. Sensitivity analysis schemes of parameters based on the base model.

Parameter	Base value	Sensitivity variation level	Analysis parameters
CO_2 injection rate (sm^3/day)	5,000	8,000, 10,000	Bottom-hole flowing pressure of the injection well; Gas production rate of the production well; Gas saturation distribution in the first reservoir layer.
Liquid production rate (sm^3/day)	30	20, 40	Bottom-hole flowing pressure of the production well; Gas production rate of the production well; Gas saturation distribution in the first reservoir layer.
Porosity	Layer 1: 0.18 Layer 2: 0.20 Layer 3: 0.22	Layer 1: 0.144, 0.216 Layer 2: 0.160, 0.240 Layer 3: 0.176, 0.264	Current oil in place; Bottom-hole flowing pressure of the production well; Gas saturation distribution in the first reservoir layer.
Streak permeability (mD)	Layer 1: 500 Layer 2: 650 Layer 3: 350	Layer 1: 250, 1,000 Layer 2: 325, 1,300 Layer 3: 175, 700	Bottom-hole flowing pressure of the injection well; Gas production rate of the production well; Gas saturation distribution in the first reservoir layer.

4.1. Sensitivity analysis of CO_2 injection rate

Based on Case 1, Case 2 was simulated under two constant CO_2 injection rates of 8,000 sm^3/day and 10,000 sm^3/day, respectively. The production well was operated at a constant liquid production rate of 30 sm^3/day, while all other model parameters remained identical to those of Case 1.

Figure 5 shows the injection-well bottom-hole flowing pressure under different CO_2 injection rates. At 5,000 sm^3/day, the pressure decreased rapidly initially and more gradually after approximately 200 days, indicating sufficient reservoir injectivity and a relatively low pressure requirement for maintaining the prescribed rate. When the injection rate was increased to 8,000 sm^3/day, the bottom-hole flowing pressure remained significantly higher than that of the base case throughout most of the simulation and began to decrease gradually after approximately 1,200 days of production. With a further increase in the injection rate to 10,000 sm^3/day, the bottom-hole flowing pressure reached the highest level and started to decline after peaking at approximately 1,000 days. These results indicate that, under constant-rate injection control, a higher CO_2 injection rate requires a higher bottom-hole flowing pressure to overcome the reservoir flow resistance and sustain the prescribed injection rate. The subsequent decline in bottom-hole flowing pressure indicates that, as CO_2 progressively migrated through the reservoir, preferential flow channels were gradually established, resulting in enhanced reservoir injectivity and a lower bottom-hole flowing pressure required to maintain the same injection rate. This pressure plateau followed by a decline is broadly consistent with Wang et al. [17], who identified injection pressure and permeability contrast as important controls on CO_2 miscible-flooding behavior; in the present model, the plateau represents the pressure required to maintain the imposed rate before the connected high-permeability pathway improves injectivity.

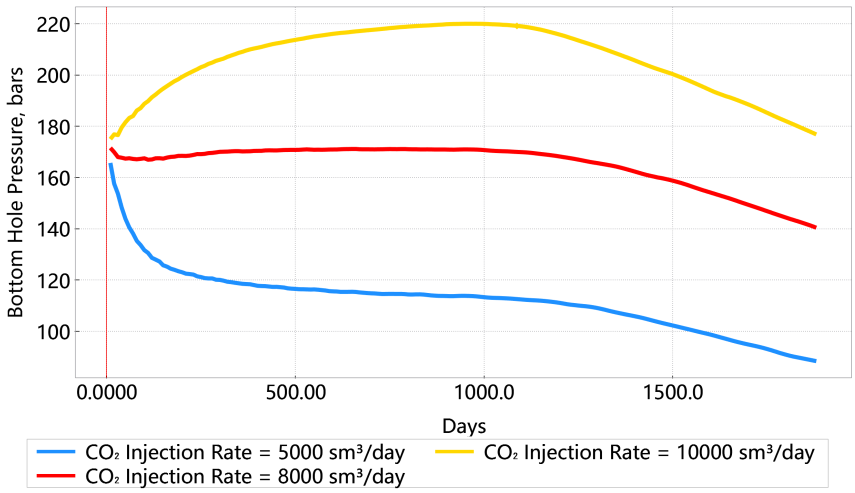

Figure 5. Bottom-hole flowing pressure curves of the injection well under different CO_2 injection rate scenarios.

Figure 6 presents the variation in the gas production rate of the production well under different CO_2 injection rates. As shown in **Figure 6**, the gas production rate remained at a relatively low level during the early production stage for all injection scenarios and began to increase significantly after approximately 900 days, indicating that the injected CO_2 front had gradually reached the vicinity of the production well. Under the injection rate of 5,000 sm^3/day, the gas production rate increased relatively slowly and remained the lowest during the late production stage. As the CO_2 injection rate increased, both the gas production rate and its growth rate during the late production stage became progressively higher. These results indicate that, under the same liquid production rate, increasing the CO_2 injection rate enhances the displacement capacity of the injected gas within the reservoir, allowing CO_2 to migrate more readily along the high-permeability channel, thereby increasing the degree of gas breakthrough and the risk of gas channeling at the production well.

Figures 7 and **8** present the gas saturation and oil-phase CO_2 mole-fraction (XMFCO$_2$) distributions, respectively, in the first reservoir layer under different CO_2 injection rates. At 1,200 days, the free-gas region under 5,000 sm^3/day had advanced along the injection–production direction, whereas the corresponding regions under 8,000 sm^3/day and 10,000 sm^3/day remained more concentrated near the injection well. By 1,880 days, the free-gas front had reached the production well in all cases, with stronger near-well accumulation at higher injection rates. In contrast, the XMFCO_2 fields show that, within the oil-containing region, values were predominantly approximately 0.37–0.55 in the 5,000 sm^3/day case, whereas extensive regions with values of approximately 0.55–0.74 developed in the 8,000 sm^3/day and 10,000 sm^3/day cases. This comparison demonstrates that increasing the injection rate enhances CO_2 enrichment in the oil phase, although the free-gas phase in the first layer does not expand proportionally. Because XMFCO_2 is an oil-phase composition variable rather than a measure of the phase-specific CO_2 inventory, the gas-saturation and XMFCO_2 fields are interpreted jointly to distinguish the spatial responses of free-gas and oil-dissolved CO_2.

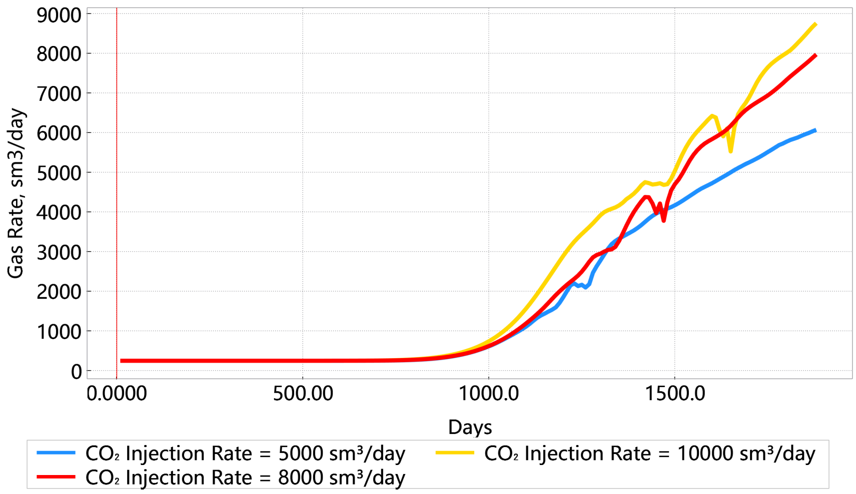

Figure 6. Gas production rate curves of the production well under different CO_2 injection rate scenarios.

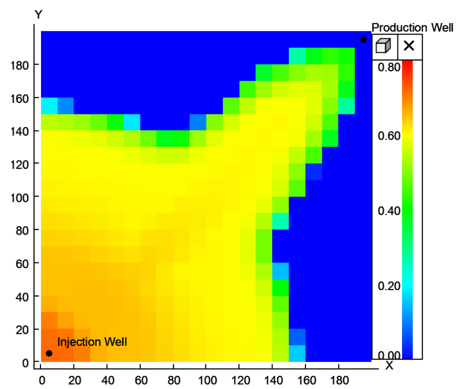

(a) 5,000 sm^3/day, 1,200 d.

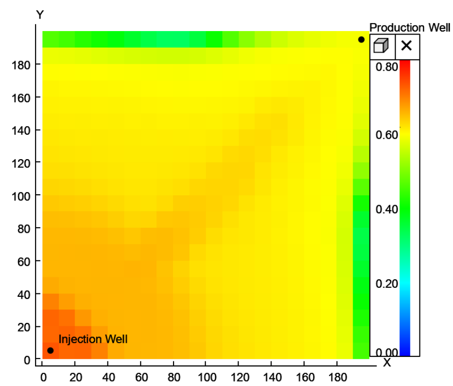

(b) 5,000 sm^3/day, 1,880 d.

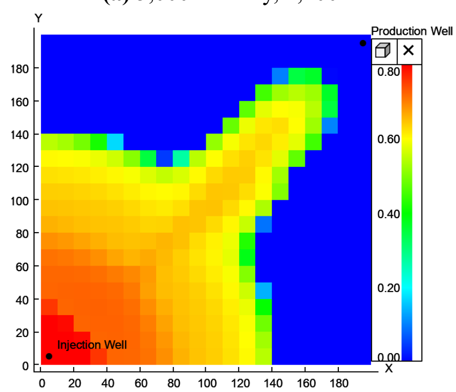

(c) 8,000 sm^3/day, 1,200 d.

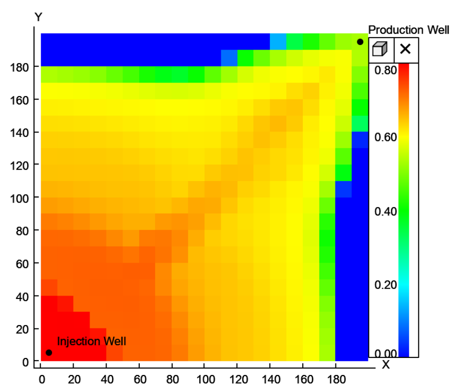

(d) 8,000 sm^3/day, 1,880 d.

Figure 7. *Cont.*

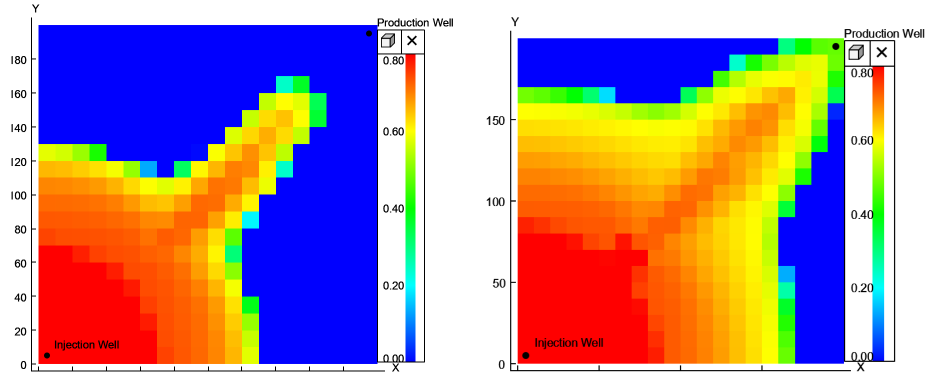

(e) 10,000 sm^3/day, 1,200 d. **(f)** 10,000 sm^3/day, 1,880 d.

Figure 7. Gas saturation distribution in the first reservoir layer under different CO_2 injection rate scenarios.

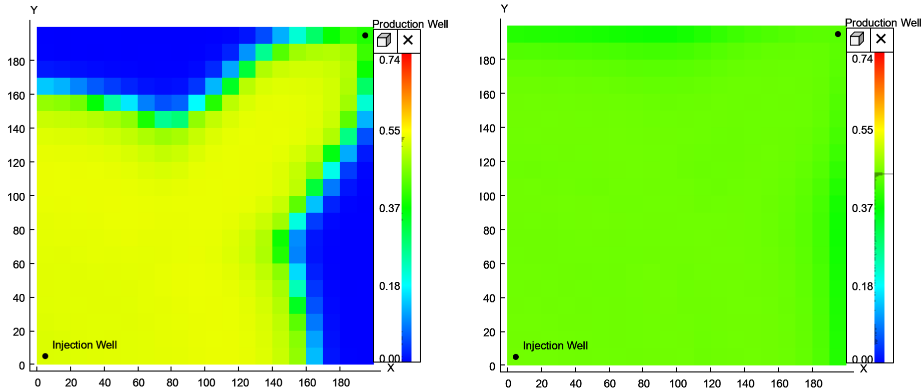

(a) 5,000 sm^3/day, 1,200 d. **(b)** 5,000 sm^3/day, 1,880 d.

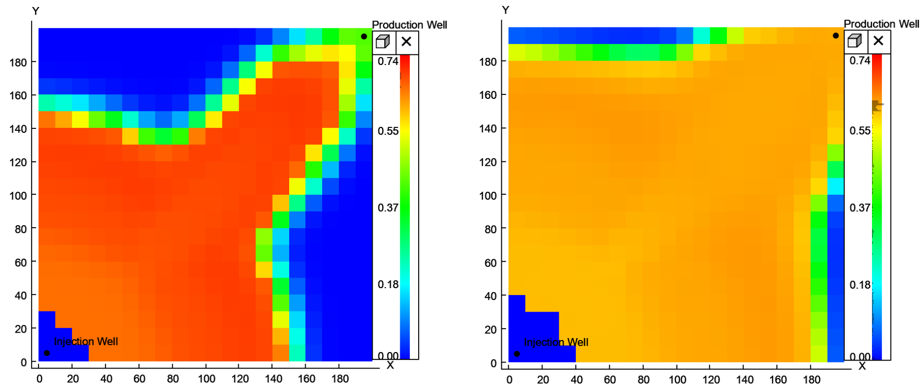

(c) 8,000 sm^3/day, 1,200 d. **(d)** 8,000 sm^3/day, 1,880 d.

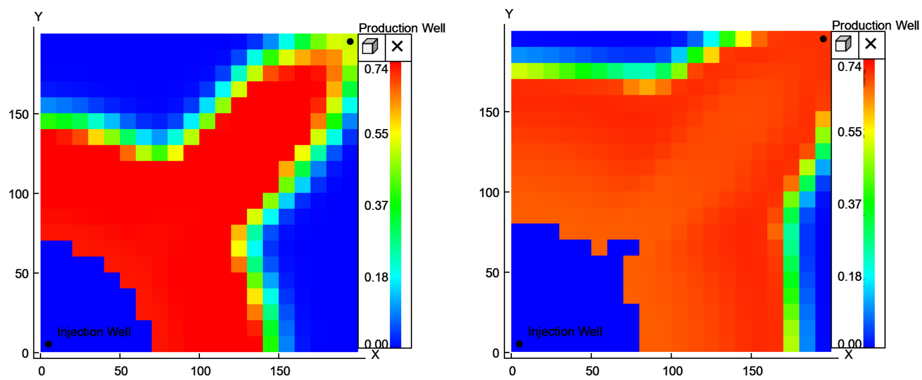

(e) 10,000 sm^3/day, 1,200 d. **(f)** 10,000 sm^3/day, 1,880 d.

Figure 8. Oil-phase CO_2 mole-fraction ($XMFCO_2$) distributions in the first reservoir layer under different CO_2 injection-rate scenarios.

In summary, the CO_2 injection rate has a significant influence on the wellbore-reservoir coupled response and CO_2 migration behavior. With the liquid production rate maintained at 30 sm^3/day, increasing the injection rate from 5,000 sm^3/day to 8,000 sm^3/day and 10,000 sm^3/day increased the bottom-hole flowing pressure required to maintain the prescribed injection rate. Meanwhile, both the gas production rate and its late-stage growth rate increased with the injection rate. The combined gas-saturation and $XMFCO_2$ distributions show that higher injection rates produced stronger local free-gas accumulation in the first reservoir layer and greater CO_2 enrichment in the remaining oil phase. Thus, the free-gas phase and oil-dissolved CO_2 exhibited distinct spatial responses to injection intensity. Overall, increasing the CO_2 injection rate enhances pressure support and CO_2 transport, but also increases gas production and the risk of gas channeling at the production well.

4.2. Sensitivity analysis of production well liquid production rate

Based on Case 1, Case 2 was simulated under two constant liquid production rates of 20 sm^3/day and 40 sm^3/day, respectively. The injection well was maintained at a constant CO_2 injection rate of 5000 sm^3/day, while all other parameters remained identical to those of Case 1.

Figure 9 presents the variation in the bottom-hole flowing pressure of the production well over time under different liquid production rates. As shown in **Figure 9**, when the liquid production rate was 20 sm^3/day, the bottom-hole flowing pressure of the production well remained stable at approximately 155 bar and decreased slightly during the late production stage. This indicates that under a relatively low production intensity, the reservoir fluid supply capacity could adequately meet the production demand, resulting in weaker pressure depletion around the production well. When the liquid production rate was increased to 30 sm^3/day, the decline in bottom-hole flowing pressure became significantly greater, indicating that as more fluids were produced, the formation pressure around the production well decreased more substantially, and a larger production pressure differential was required to maintain the higher liquid production rate, thereby causing a further reduction in bottom-hole flowing pressure. When the liquid production rate was further increased to 40 sm^3/day, the bottom-hole flowing pressure decreased rapidly during the first 200 days of production and continued to decline thereafter, indicating that pressure depletion around the production well was significantly intensified under high liquid production conditions. Overall, the bottom-hole flowing pressure under all three liquid production rate scenarios exhibited an accelerated decline during the late production stage. This is because as gas migrated along the channel and reached the production well, the gas content in the production well increased significantly, resulting in a decrease in the relative permeability of the liquid phase. Under the constraint of a fixed liquid production rate, the calculated bottom-hole flowing pressure was therefore further reduced.

Figure 10 shows the production-well gas rate under different liquid production rates at a fixed CO_2 injection rate of 5,000 sm^3/day, with a stronger late-stage increase at higher liquid rates. When the liquid production rate was 20 sm^3/day, the gas production rate remained at a relatively low level for a long period. Although it increased after

1,300 days of production, the overall increase was relatively limited, indicating that under a low liquid production intensity, the production well exerted a weaker driving effect on gas migration, and the advancement of CO_2 toward the production well was relatively slow. When the liquid production rate was 30 sm^3/day, the gas production rate began to increase significantly after approximately 900 days of production, reaching a maximum value of 6×10^3 sm^3/day. This indicates that increasing the liquid production rate enhanced the tendency of gas migration toward the production well. When the liquid production rate was increased to 40 sm^3/day, gas production began rising rapidly at approximately 600 days and reached approximately 1.5×10^4 sm^3/day, indicating that the stronger production intensity promoted CO_2 migration along the high-permeability channel and caused earlier gas breakthrough.

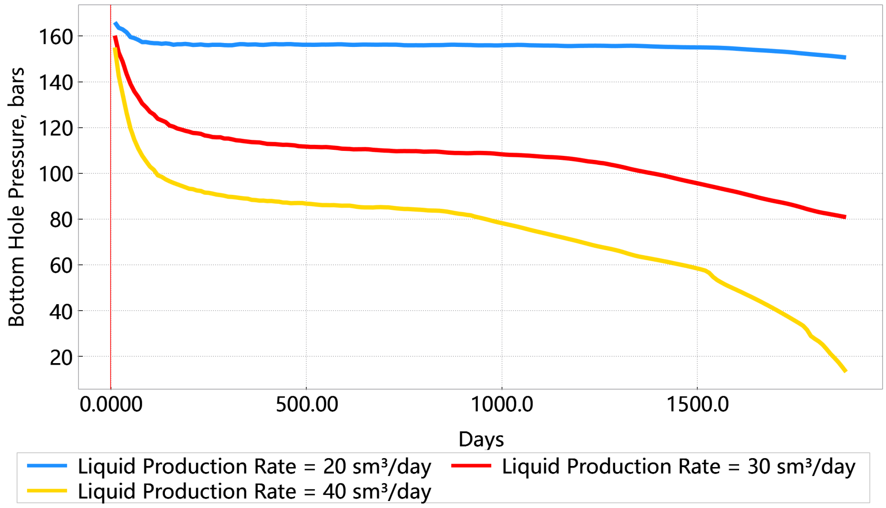

Figure 9. Bottom-hole flowing pressure curves of the production well under different liquid production rate scenarios.

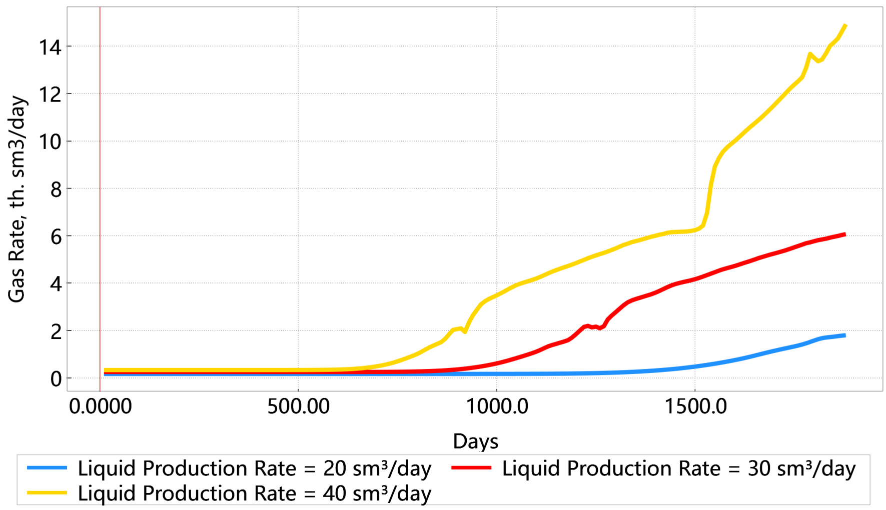

Figure 10. Gas production rate curves of the production well under different liquid production rate scenarios.

Figure 11 presents the gas saturation distribution in the first reservoir layer under different liquid production rates. As shown in **Figure 11**, with increasing liquid production rate, the distribution range of gas saturation in the first layer gradually expanded, and the high gas saturation region extended from the vicinity of the injection well toward the production well. By comparing the gas saturation distribution at 1,200 days of production, it can be observed that increasing the liquid production rate significantly enlarged the propagation range of the gas front. At 1,880 days, the gas-bearing regions of all cases further expanded, among which the case with a liquid production rate of 40 sm^3/day exhibited the widest high gas saturation region.

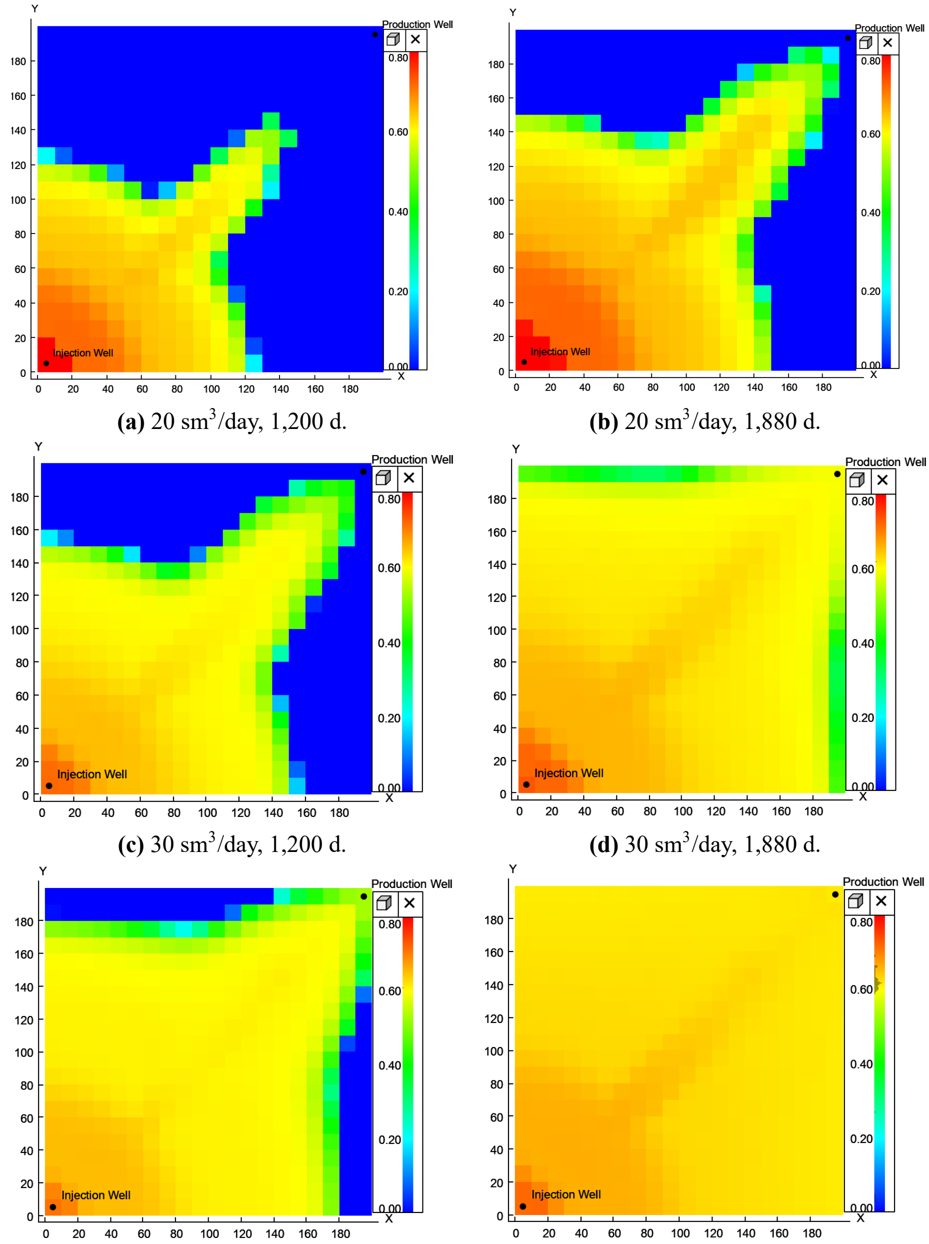

(a) 20 sm^3/day, 1,200 d. **(b)** 20 sm^3/day, 1,880 d.
(c) 30 sm^3/day, 1,200 d. **(d)** 30 sm^3/day, 1,880 d.
(e) 40 sm^3/day, 1,200 d. **(f)** 40 sm^3/day, 1,880 d.

Figure 11. Gas saturation distribution in the first reservoir layer under different liquid production rate scenarios.

At a fixed CO_2 injection rate of 5,000 sm^3/day, increasing the liquid production rate from 20 sm^3/day to 40 sm^3/day reduced the final production-well bottom-hole flowing pressure from approximately 150 bar to approximately 13 bar, advanced gas breakthrough from approximately 1,100 days to approximately 700 days, and increased the final gas production rate from approximately 1.8×10^3 sm^3/day to approximately 1.5×10^4 sm^3/day. The gas saturation distribution further indicates that the gas front propagated faster and the high gas saturation region between the injection and production wells became larger under the high liquid production rate scenario, demonstrating that increasing the production intensity enhanced the pressure-driven attraction of the production well to CO_2. Therefore, although increasing the liquid production rate can improve fluid recovery capacity, when the liquid production rate reaches 40 sm^3/day, the excessively low bottom-hole flowing pressure and significantly earlier gas appearance indicate that the risk of gas channeling increases substantially.

4.3. Sensitivity analysis of porosity

Based on Case 1, two models with porosity values of 0.8 and 1.2 times those of Case 1 were established in Case 2 for simulation. The CO_2 injection and liquid production rates were fixed at 5,000 sm^3/day and 30 sm^3/day, respectively, while all other parameters remained as in Case 1.

Figure 12 shows current oil in place under different porosity conditions, with initial values of approximately 94 × 10^3 sm^3, 118 × 10^3 sm^3, and 141 × 10^3 sm^3 for the low-porosity, base-case, and high-porosity scenarios, respectively. A higher porosity resulted in a larger reservoir pore volume and higher initial oil in place. After 1,880 days of production, the current oil in place for the three scenarios decreased to approximately 35 × 10^3 sm^3, 59 × 10^3 sm^3, and 82 × 10^3 sm^3, respectively, with the cumulative oil consumption being approximately 59 × 10^3 sm^3 for all cases. The three curves exhibited an approximately linear decline trend, indicating that under constant CO_2 injection rate and liquid production rate conditions, the oil depletion process remained relatively stable for all scenarios.

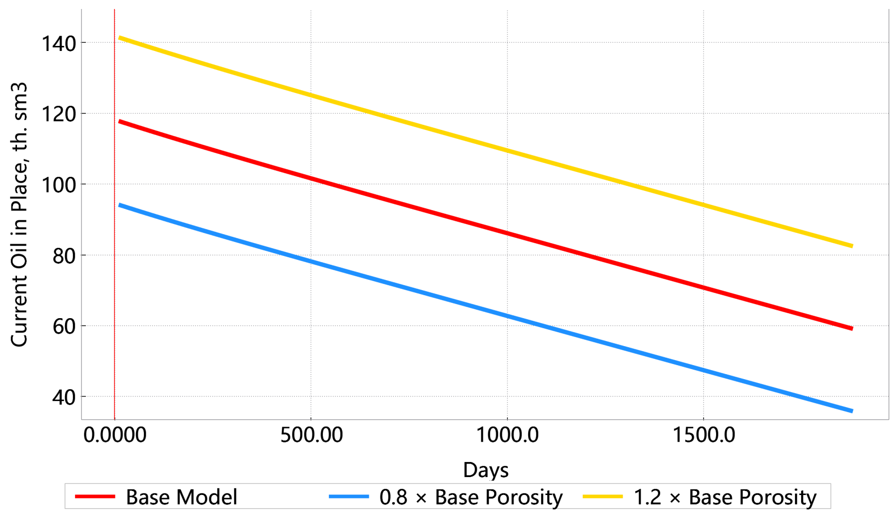

Figure 12. Current oil in place under different porosity conditions.

Figure 13 presents the bottom-hole flowing pressure of the production well under different porosity conditions. As shown in **Figure 13**, the bottom-hole flowing pressure decreased rapidly during the early production stage, reaching approximately 116–120 bar at 200 days, after which the decline rate gradually slowed. After 800 days of production, the bottom-hole flowing pressures of different scenarios gradually diverged. At the end of production, the bottom-hole flowing pressures of the low-porosity, base-case, and high-porosity scenarios were approximately 52 bar, 80 bar, and 93 bar, respectively. The low-porosity scenario exhibited the largest pressure decline, whereas the high-porosity scenario showed the smallest decline. This indicates that under the same CO_2 injection rate and liquid production rate conditions, a reduction in porosity weakens the reservoir storage capacity and pressure-buffering capability, whereas an increase in porosity enhances the reservoir fluid supply capacity, allowing the bottom-hole flowing pressure to be maintained at a higher level.

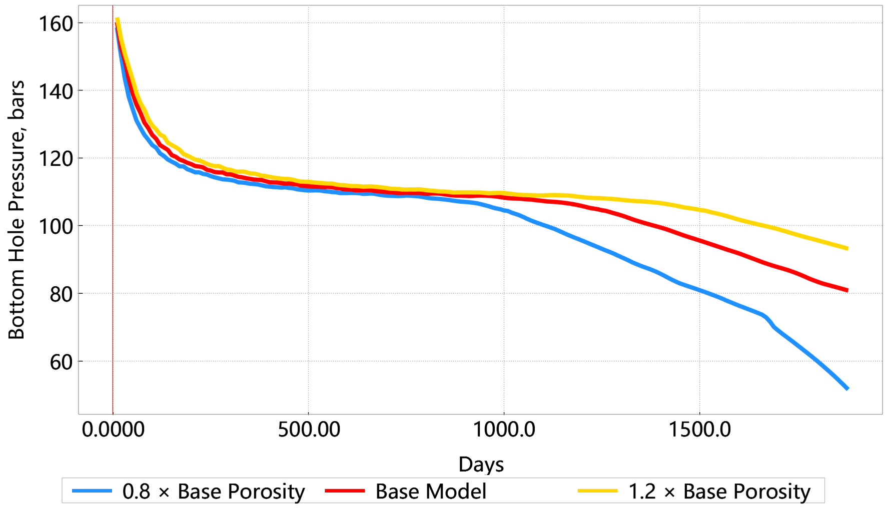

Figure 13. Bottom-hole flowing pressure curves of the production well under different porosity scenarios.

Figure 14 presents the spatial distribution of gas saturation in the first reservoir layer for different porosity scenarios at 1,200 days and 1,880 days of production. As the production time increased, CO_2 continuously migrated from the injection well toward the production well, and the high gas saturation region gradually expanded. At the same production time, the 0.8-times porosity scenario exhibited the fastest gas-front propagation and had already affected the entire layer at 1,880 days. The base-case model showed the second-fastest propagation, whereas the 1.2-times porosity scenario still contained relatively obvious unswept regions. This indicates that a decrease in porosity increases the CO_2 injection intensity corresponding to a unit pore volume, thereby accelerating CO_2 propagation; whereas an increase in porosity enhances the reservoir's gas storage capacity, resulting in relatively slower gas-front propagation.

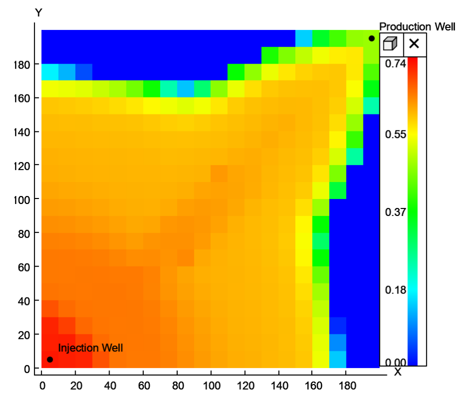

(a) 0.8 times porosity, 1,200 d.

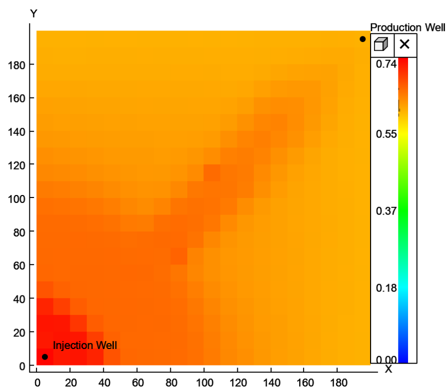

(b) 0.8 times porosity, 1,880 d.

Figure 14. *Cont.*

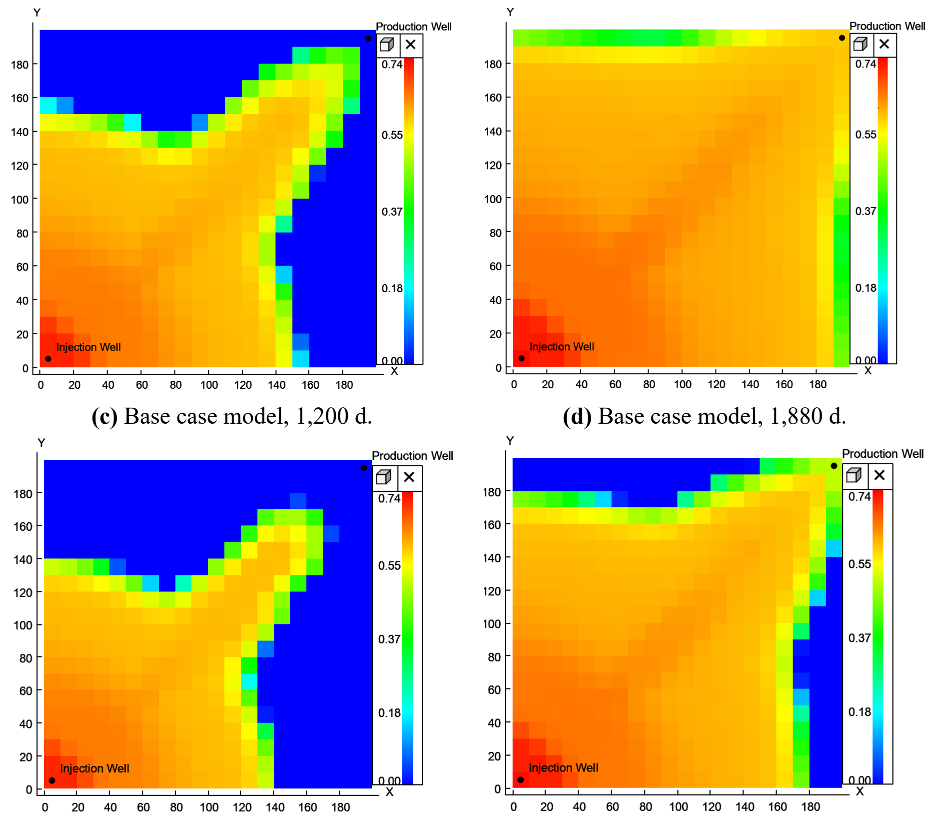

(c) Base case model, 1,200 d. **(d)** Base case model, 1,880 d.

(e) 1.2 times porosity, 1,200 d. **(f)** 1.2 times porosity, 1,880 d.

Figure 14. Gas saturation distribution in the first reservoir layer under different porosity scenarios.

A comprehensive analysis indicates that porosity has a significant influence on oil in place, pressure variation, and CO_2 migration. When the porosity increased from 0.8 times the base value to 1.2 times the base value, the initial oil in place increased from approximately 94 × 10^3 sm^3 to 141 × 10^3 sm^3, and the bottom-hole flowing pressure of the production well at the end of production increased from approximately 52 bar to 93 bar. Meanwhile, increasing porosity slowed the propagation of the CO_2 front, which was beneficial for extending the gas breakthrough time. Overall, higher porosity enhanced the reservoir storage capacity and pressure-buffering capability, improved production stability, and reduced the risk of premature CO_2 breakthrough.

4.4. Sensitivity analysis of streak permeability multiplier

Based on Case 1, two models were established in Case 2, in which the permeability of the grid blocks within the high-permeability channel was set to 5 and 20 times that of the grid blocks outside the high-permeability channel, respectively, for coupled simulations. The injection well was maintained at a constant CO_2 injection rate of 5,000 sm^3/day, and the production well was operated at a constant liquid production rate of 30 sm^3/day. All other parameters remained identical to those of Case 1. In this study, streak permeability denotes the permeability assigned to the grid blocks within the continuous high-permeability channel and corresponds to “Streak Permeability” in the simulation-output figures.

Figure 15 shows similar injection-well bottom-hole flowing pressure trends across all streak-permeability scenarios during the first 800 days, followed by gradually increasing differences. At 1,880 days of production, the bottom-hole flowing pressures of the low-permeability, base-case, and high-permeability scenarios were approximately 98 bar, 88 bar, and 81 bar, respectively. This indicates that under the condition of a constant CO_2 injection rate of 5,000 sm^3/day, increasing the streak permeability can reduce the flow resistance of CO_2, thereby lowering the bottom-hole flowing pressure required to maintain the same injection rate.

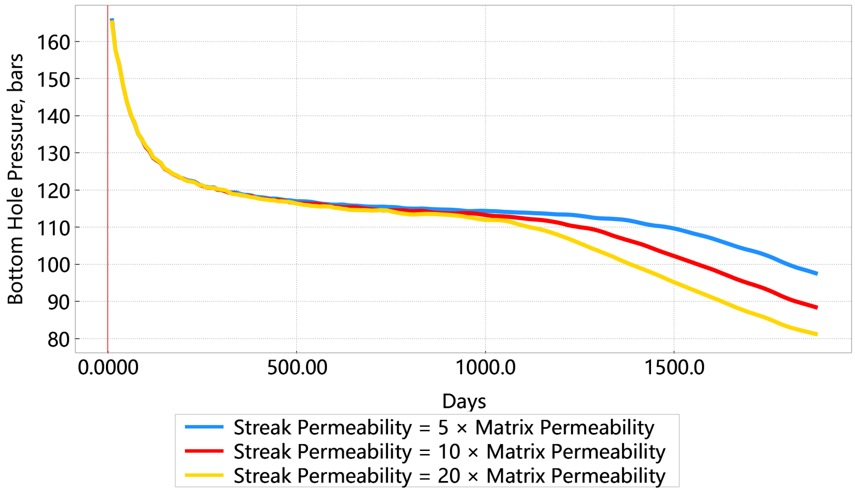

Figure 15. Bottom-hole flowing pressure curves of the injection well under different streak-permeability scenarios.

Figure 16 shows that gas production remained near 250 sm^3/day in all streak-permeability scenarios during the first 800 days before increasing rapidly at different times. The gas production rates of the high-permeability, base-case, and low-permeability scenarios began to increase significantly after approximately 900 days, 1,000 days, and 1,100 days, respectively, indicating that a higher streak permeability resulted in faster CO_2 migration along the preferential flow path between the wells and earlier gas breakthrough at the production well. At the end of production, the gas production rates of all scenarios approached 6,000 sm^3/day; however, the high-permeability scenario exhibited a more pronounced early gas breakthrough characteristic during the middle production stage.

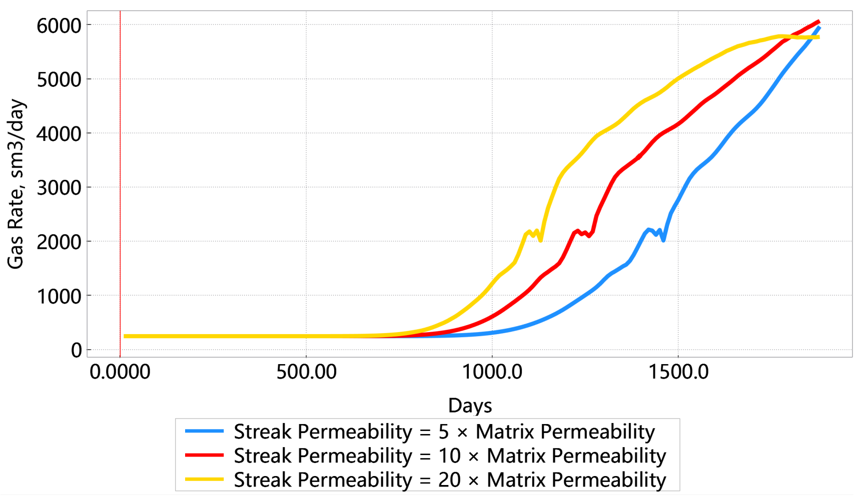

Figure 16. Gas production rate variation curves under different streak-permeability scenarios.

Figure 17 presents the gas saturation distribution in the first reservoir layer for different streak-permeability multiplier scenarios at 1,200 days and 1,880 days of production. At 1,200 days, the gas front in the low-permeability scenario remained far from the production well, whereas higher permeability extended the gas-bearing region along the high-permeability streak and brought the front close to the production well. By 1,880 days, all gas-bearing regions had expanded, with a more pronounced high-gas-saturation channel between the wells in the high-permeability scenario. The results indicate that increasing the streak permeability strengthens the preferential flow path effect, accelerates the directional migration of CO_2, and simultaneously reduces the uniformity of the displacement front. This trend is consistent with Luo et al. [35], who reported that permeability heterogeneity alters CO_2-front morphology, sweep efficiency, and breakthrough time; the present comparison further isolates the effect of a connected high-permeability pathway by varying only its permeability multiplier.

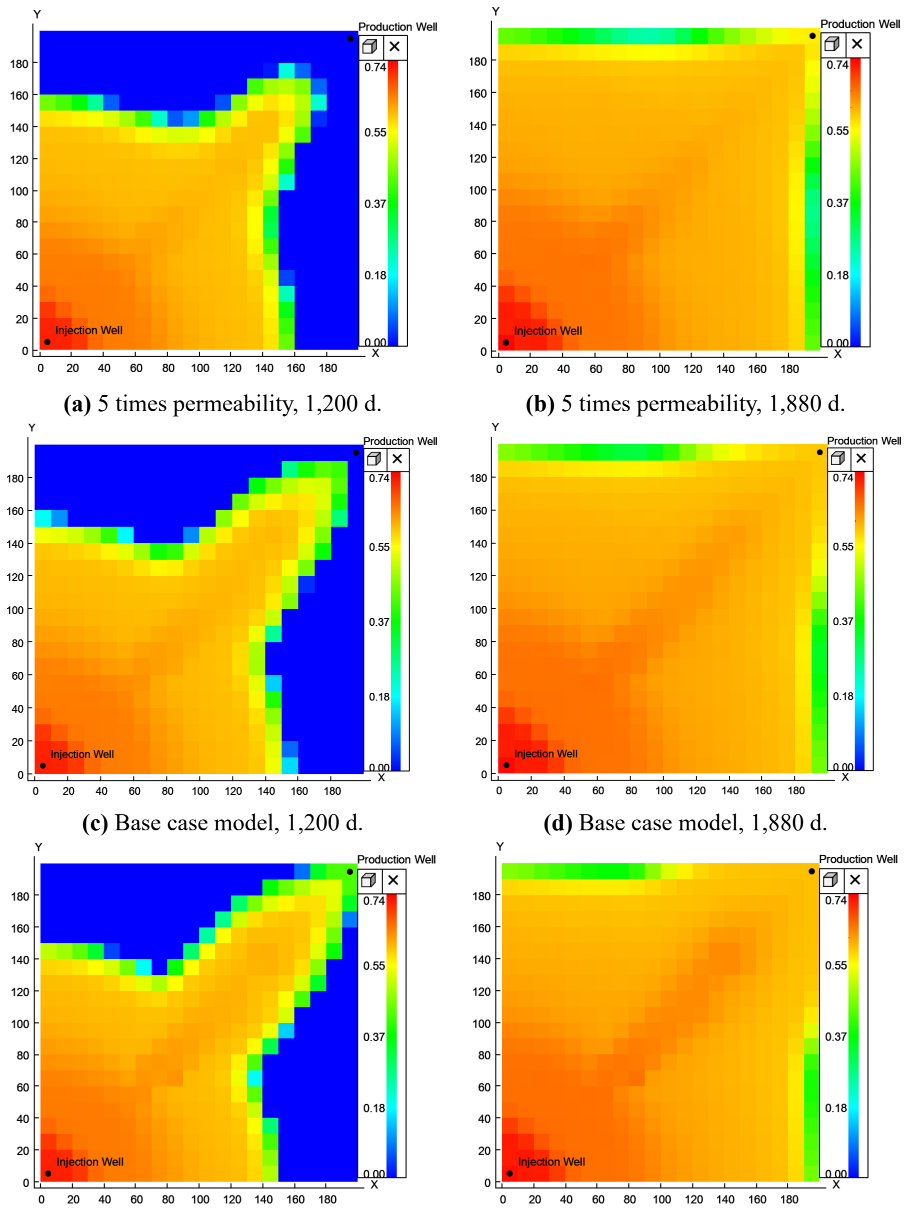

(a) 5 times permeability, 1,200 d. **(b)** 5 times permeability, 1,880 d.

(c) Base case model, 1,200 d. **(d)** Base case model, 1,880 d.

(e) 20 times permeability, 1,200 d. **(f)** 20 times permeability, 1,880 d.

Figure 17. Gas saturation distribution in the first reservoir layer under different streak-permeability scenarios.

A comprehensive analysis indicates that the streak-permeability multiplier has a significant influence on injection pressure, CO_2 propagation rate, and gas breakthrough behavior at the production well. When the streak permeability increased from 5 times to 20 times that of the surrounding reservoir, the bottom-hole flowing pressure of the injection well at the end of production decreased by approximately 17 bar, and the time when the gas production rate of the production well increased significantly was advanced by approximately 200 days. A higher streak permeability improves the CO_2 injection and migration capacity, but it also strengthens the preferential flow path between the wells, increasing the risk of premature gas breakthrough and uneven sweep. Because the high-permeability channel was represented as a straight and vertically continuous pathway, the simulated advancement of gas breakthrough may be greater than that in reservoirs containing discontinuous or tortuous high-permeability features. Therefore, the quantitative results should not be directly generalized to all heterogeneous reservoirs.

4.5. CO_2 storage performance

CO_2 storage performance was evaluated using net reservoir retention together with the free-gas and oil-phase composition distributions. Because explicit structural closure and hysteretic residual trapping were not included in the present model, structural and residual trapping were not quantified separately. **Table 7** summarizes the cumulative CO_2 injection, cumulative CO_2 production, stored CO_2, and storage efficiency under different simulation scenarios.

Table 7. CO_2 storage performance under different simulation scenarios.

Simulation scenario	Cumulative CO_2 injection (10^3 sm^3)	Cumulative CO_2 production (10^3 sm^3)	Stored CO_2 (10^3 sm^3)	Storage efficiency
Base case	9,400	3,443.270	5,956.730	63.369%
Injection rate: 8,000 sm^3/day	15,040	4,041.870	10,998.130	73.126%
Injection rate: 10,000 sm^3/day	18,800	4,530.530	14,269.470	75.901%
Liquid production rate: 20 sm^3/day	9,400	715.354	8,684.646	92.390%
Liquid production rate: 40 sm^3/day	9,400	7,624.470	1,775.530	18.889%
Porosity: 0.8 × base value	9,400	6,006.590	3,393.410	36.100%
Porosity: 1.2 × base value	9,400	2,105.840	7,294.160	77.597%
Streak permeability: 5 × matrix permeability	9,400	2,522.880	6,877.120	73.161%
Streak permeability: 20 × matrix permeability	9,400	4,171.810	5,228.190	55.619%

Table 7 summarizes the cumulative CO_2 injection, cumulative CO_2 production, stored CO_2, and storage efficiency under different simulation scenarios. In the base case, the cumulative stored CO_2 was $5,956.730 \times 10^3$ sm^3, corresponding to a storage efficiency of 63.369%. As the injection rate increased from 5,000 sm^3/day to 8,000 sm^3/day and 10,000 sm^3/day, the cumulative stored CO_2 increased to $10,998.130 \times 10^3$ sm^3 and $14,269.470 \times 10^3$ sm^3, respectively, while the storage efficiency increased to 73.126% and 75.901%. Although cumulative CO_2 production also increased, its increase was smaller than that of cumulative injection, resulting in greater net CO_2 retention within the simulated period.

Under the same cumulative CO_2 injection of $9,400 \times 10^3$ sm^3, storage performance was strongly affected by the liquid production rate, reservoir porosity, and streak permeability. Decreasing the liquid production rate to 20 sm^3/day reduced cumulative CO_2 production to 715.354 × 10^3 sm^3 and increased the storage efficiency to 92.390%, whereas increasing the liquid production rate to 40 sm^3/day reduced the storage efficiency to 18.889%. Increasing the reservoir porosity from 0.8 times to 1.2 times the base value increased the storage efficiency from 36.100% to 77.597%, indicating that greater pore volume enhanced CO_2 retention. In contrast, increasing the streak permeability from 5 times to 20 times the matrix permeability reduced the storage efficiency from 73.161% to 55.619%, because the stronger preferential-flow pathway increased CO_2 production from the production well. Overall, lower liquid production rates, larger reservoir porosity, and weaker high-permeability channeling were favorable for improving CO_2 retention during the simulated period.

5. Case 3: Analysis of wellbore-reservoir coupled response under fixed tubing-head-pressure control mode

5.1. Model setup and control strategy

In this case, only the control strategy of the injection and production wells was changed based on Case 1. The injection well was operated under fixed tubing-head-pressure control, with the tubing-head pressure set to 140 bar. The production well was also operated under fixed tubing-head-pressure control, with the tubing-head pressure set to 90 bar. The simulation period was 430 days, with a time step of 5 days. Under this control mode, the model characterized the wellbore pressure drop using VFP tables. The bottom-hole flowing pressures of the injection and production wells were obtained through interpolation based on the tubing-head pressure, well flow rate, and fluid state within the wellbore, and were coupled with the reservoir flow equations to solve for the actual CO_2 injection rate and liquid production rate.

5.2. Injection well response under fixed tubing-head-pressure control

Figure 18 presents the bottom-hole flowing pressure curve of the injection well under fixed tubing-head-pressure control, and **Figure 19** presents the CO_2 injection rate curve of the injection well under fixed tubing-head-pressure control. As shown in **Figures 18** and **19**, with the tubing-head pressure of the injection well maintained at 140 bar, the bottom-hole flowing pressure of the injection well remained at approximately 174 bar overall. This is because the injected fluid in the wellbore was pure CO_2 gas, and the wellbore pressure-drop relationship changed insignificantly; therefore, the bottom-hole injection pressure obtained from the VFP table remained relatively stable. Compared with the variation in bottom-hole flowing pressure, the dynamic characteristics of the actual injection rate were more pronounced. During the early production stage, the injection rate fluctuated slightly around 26 × 10^3 sm^3/day and then remained relatively stable from approximately 50 to 300 days, indicating that the CO_2 injectivity of the reservoir changed only slightly during this period. After 300 days, the CO_2 injection rate increased continuously and reached approximately 45 × 10^3 sm^3/day at 430 days. Because the tubing-head pressure and bottom-hole injection pressure remained nearly constant, this increase primarily reflects the evolution of reservoir injectivity. As CO_2 accumulated around the injection well, the gas relative permeability and total fluid mobility in the near-well region increased, allowing a higher injection rate to be sustained under approximately unchanged pressure conditions.

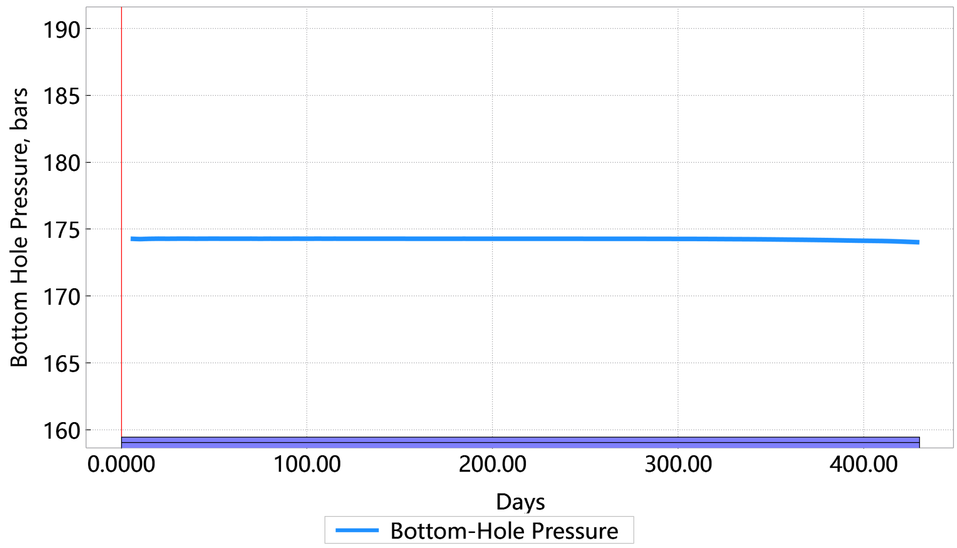

Figure 18. Bottom-hole flowing pressure curve of the injection well under fixed tubing-head-pressure control.

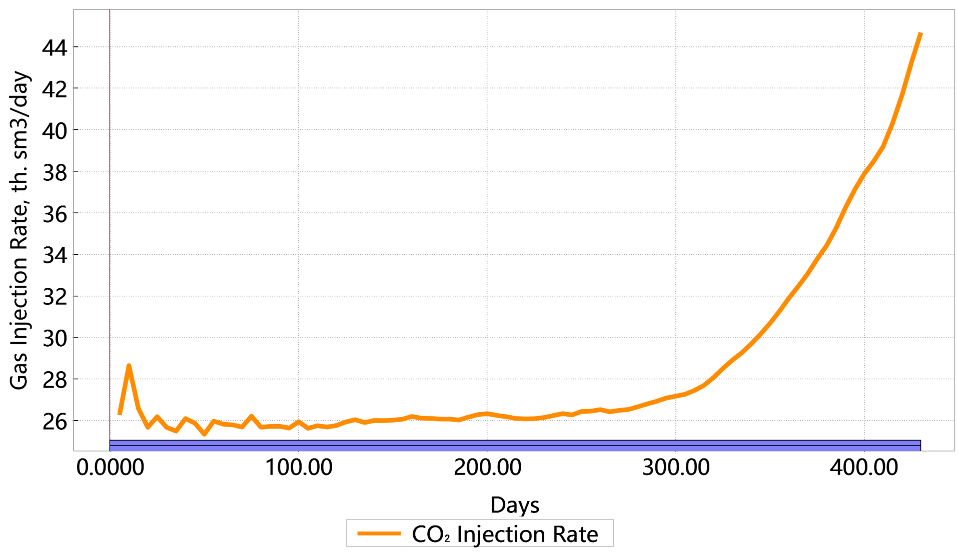

Figure 19. Injection rate curve of the injection well under fixed tubing-head-pressure control.

5.3. Production well response under fixed tubing-head-pressure control

Figure 20 presents the bottom-hole flowing pressure curve of the production well under fixed tubing-head-pressure control. As shown in **Figure 20**, with the tubing-head pressure of the production well maintained at 90 bar, the bottom-hole flowing pressure of the production well remained approximately 157 bar during the early production stage, indicating that the fluid state within the wellbore and the wellbore pressure-drop relationship were relatively stable at the initial production stage. After 250 days of production, the bottom-hole flowing pressure began to decrease gradually, and the declining trend became more apparent after 300 days, reaching approximately 145 bar at around 430 days of production. This variation was mainly related to changes in the composition of produced fluids and the multiphase flow behavior within the wellbore during the later production stage. As CO_2 gradually migrated toward the production well, the produced gas rate increased significantly, resulting in changes in the gas–liquid ratio, mixture density, liquid holdup, and frictional pressure loss within the wellbore. In this case, the reduction in gravitational pressure loss caused by the decrease in mixture density dominated the overall pressure variation. Therefore, under the condition of constant tubing-head pressure, the bottom-hole flowing pressure of the production well obtained from the VFP table exhibited an overall decreasing trend.

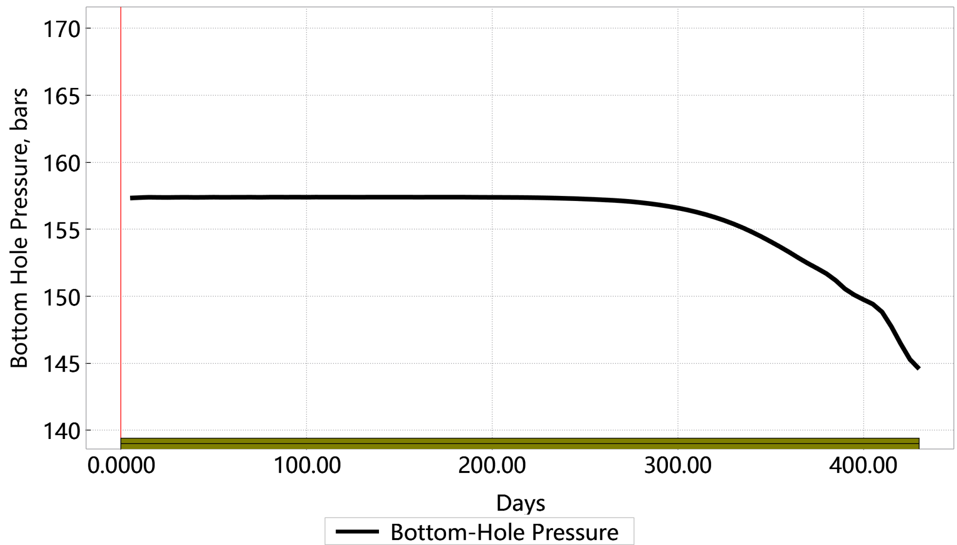

Figure 20. Bottom-hole flowing pressure curve of the production well under fixed tubing-head-pressure control.

Figure 21 presents the liquid production rate curve of the production well, and **Figure 22** presents the gas production rate curve of the production well. As shown in **Figures 21** and **22**, the gas production rate remained relatively low during the early production stage, maintaining approximately 0.8×10^3 sm^3/day, while the liquid production rate rapidly increased from approximately 78 sm^3/day at the initial stage to approximately 100 sm^3/day and then remained relatively stable during the early and middle production stages. After 300 days, both the gas and liquid production rates increased markedly. At 430 days, the gas production rate reached approximately 22×10^3 sm^3/day and the liquid production rate reached approximately 154 sm^3/day. The increase in liquid production rate should not be attributed solely to enhanced gas-phase mobility. As the produced gas–liquid ratio increased, the mixture density, liquid holdup, and pressure loss in the production well changed, causing the bottom-hole flowing pressure converted from the fixed tubing-head pressure to decrease from approximately 157 bar to 145 bar. The resulting increase in reservoir drawdown, together with changes in near-well fluid mobility following CO_2 arrival, produced the observed increase in liquid production rate.

Gas relative permeability directly affects gas-phase mobility and consequently influences the pressure and rate responses of the injection and production wells under fixed tubing-head-pressure control. Therefore, two additional sensitivity cases were established based on Case 3. The gas relative permeability values were set to 0.8 and 1.2 times those of the reference case, respectively, while the saturation nodes, oil relative permeability, reservoir properties, fluid model, wellbore model, and operating conditions were kept unchanged.

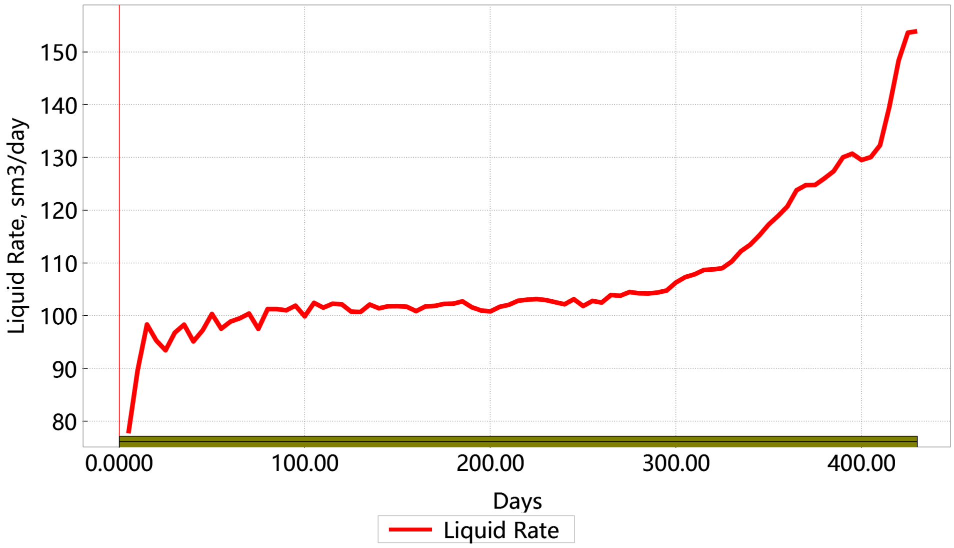

Figure 21. Liquid production rate curve of the production well under fixed tubing-head-pressure control.

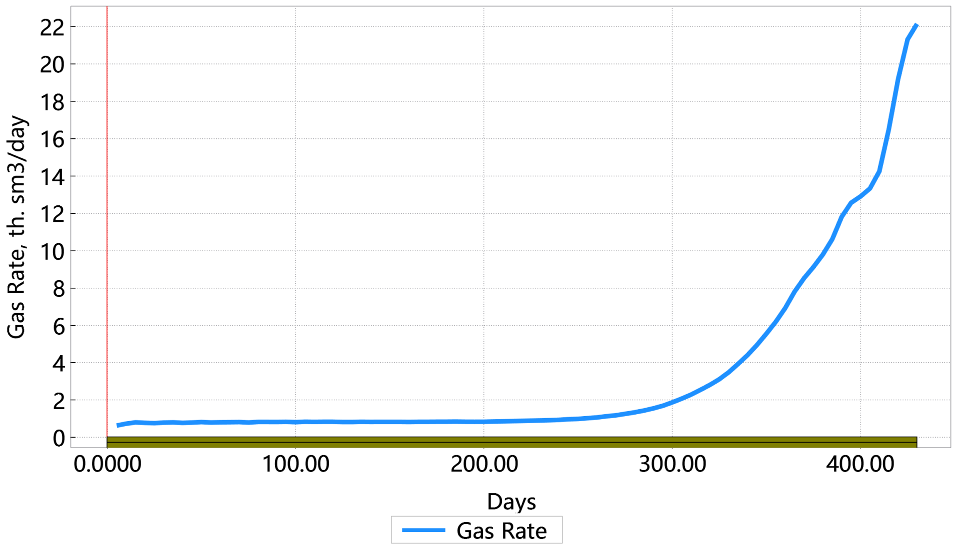

Figure 22. Gas production rate curve of the production well under fixed tubing-head-pressure control.

As shown in **Figure 23**, the late-time increases in the injection and production rates occurred earlier and became more pronounced as gas relative permeability increased. At 430 days, the CO_2 injection rates in the high-, reference-, and low-gas-relative-permeability cases were approximately 53×10^3, 45×10^3, and 35×10^3 sm^3/day, respectively, and the corresponding gas production rates were approximately 29×10^3, 22×10^3, and 12×10^3 sm^3/day. These differences indicate that a higher gas relative permeability increases the effective gas mobility in the reservoir, allowing a higher CO_2 injection rate to be maintained under the same injection-well tubing-head pressure and producing an earlier and stronger gas response at the production well.

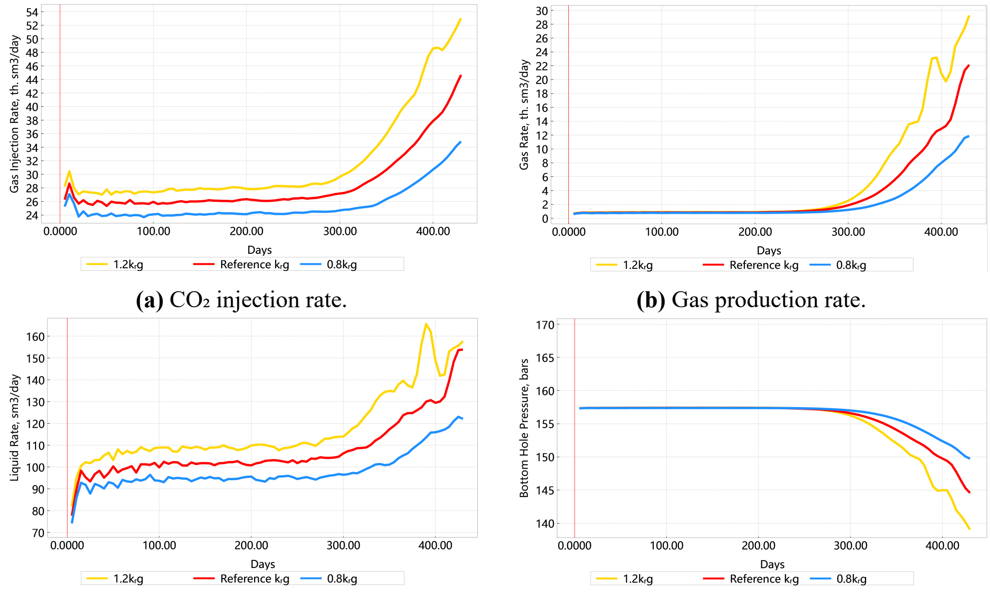

(a) CO_2 injection rate. **(b)** Gas production rate. **(c)** Liquid production rate. **(d)** Production-well bottom-hole flowing pressure.

Figure 23. Sensitivity of well responses to gas relative permeability under fixed tubing-head-pressure control.

At 430 days, the liquid production rates in the high-, reference-, and low-gas-relative-permeability cases were approximately 157, 154, and 123 sm^3/day, respectively, while the corresponding production-well bottom-hole flowing pressures were approximately 139, 145, and 151 bar. With increasing gas production, the produced gas–liquid ratio and the multiphase pressure loss represented by the VFP relationship changed. Under the fixed production-well tubing-head pressure, these changes resulted in a lower bottom-hole flowing pressure and a larger reservoir drawdown, thereby contributing to the increase in liquid production rate. Although the magnitudes and onset times of the well responses varied with gas relative permeability, all three cases exhibited increasing injection and production rates during the late production stage, demonstrating the sensitivity of the coupled wellbore-reservoir response to gas-phase mobility.

5.4. CO_2 migration and gas saturation field evolution

Figure 24 presents the gas saturation distribution in the first reservoir layer under fixed tubing-head-pressure control. As shown in **Figure 24**, at 300 days of production, CO_2 was mainly distributed around the injection well and along the direction connecting the injection and production wells. The high gas saturation region propagated from the injection well toward the production well but had not yet reached the vicinity of the production well, indicating that CO_2 was still in the stage of outward expansion and preferential flow path propagation during this period. At 430 days of production, the gas-bearing region further expanded, and the gas front had reached the production well along the direction between the injection and production wells. A relatively distinct continuous high gas saturation channel was formed between the injection and production wells.

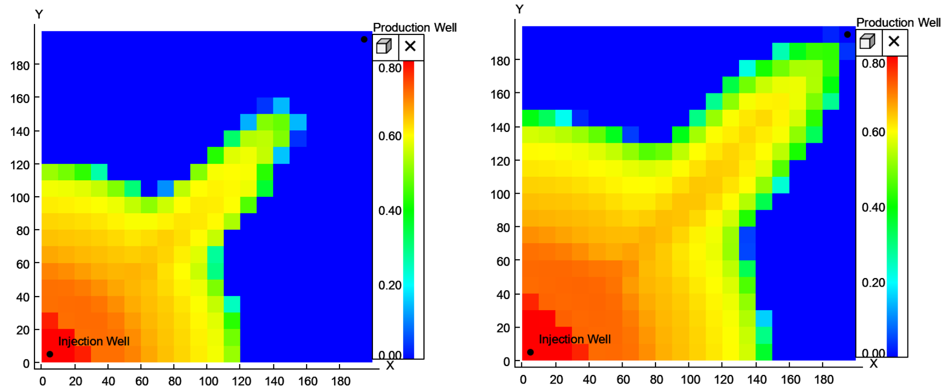

(a) 300 d. **(b)** 430 d.

Figure 24. Gas saturation distribution in the first reservoir layer under fixed tubing-head-pressure control.

5.5. CO_2 storage performance under fixed tubing-head-pressure control

Table 8 summarizes the CO_2 storage performance under fixed tubing-head-pressure control.

Table 8. CO_2 storage performance under fixed tubing-head-pressure control.

Simulation scenario	Cumulative CO_2 injection (10^3 sm^3)	Cumulative CO_2 production (10^3 sm^3)	Stored CO_2 (10^3 sm^3)	Storage efficiency
Fixed tubing-head pressure	12,211.700	1,466.410	10,745.290	87.992%

Under fixed tubing-head-pressure control, the actual CO_2 injection and production rates varied dynamically with wellbore pressure losses and reservoir injectivity and deliverability. At 430 days, the cumulative CO_2 injection reached $12{,}211.700 \times 10^3$ sm^3, whereas the cumulative CO_2 production was $1{,}466.410 \times 10^3$ sm^3. The corresponding stored CO_2 amount was $10{,}745.290 \times 10^3$ sm^3, resulting in a storage efficiency of 87.992%. Thus, only 12.008% of the injected CO_2 was produced during the simulated period, while the majority remained in the reservoir. These results indicate that the fixed tubing-head-pressure case maintained a relatively high CO_2 retention efficiency over the 430-day simulation period despite the increase in gas production during the late stage.

5.6. Comparison with the constant injection and production rate mode

Compared with the constant liquid production rate mode, the response of the production well under fixed tubing-head-pressure control can more directly reflect the coupled relationship among wellbore flow, bottom-hole boundary conditions, and reservoir dynamics. Under the constant liquid production rate mode, the liquid production rate of the production well is predetermined by the control condition, and the effects of reservoir fluid supply capacity variation and CO_2 breakthrough are mainly reflected through the decline in bottom-hole flowing pressure and the increase in gas production rate. In contrast, under the fixed tubing-head-pressure control mode, the tubing-head pressure of the production well remains constant, while the bottom-hole flowing pressure, liquid production rate, and gas production rate dynamically vary with reservoir pressure, fluid composition, and wellbore pressure-drop conditions.

Before CO_2 significantly affects the production well, the liquid production rate remains relatively stable. As CO_2 migrates along the high-permeability channel toward the vicinity of the production well, the gas-phase flow capacity increases, the fluid composition and multiphase flow behavior within the wellbore change, and the gas production rate of the production well increases rapidly, accompanied by an increase in liquid production rate. Therefore, fixed tubing-head-pressure control can reveal the coupled variations between the actual production capacity of the production well and wellbore pressure response before and after CO_2 breakthrough, making it more suitable for evaluating production performance evolution and gas channeling effects during CO_2 flooding development under tubing-head pressure conditions.

6. Conclusions

Conventional CO_2 flooding simulations often simplify wellbore flow, tubing-head-to-downhole pressure conversion, and CO_2 migration through high-permeability channels. This study developed a coupled wellbore-reservoir model in tNavigator by integrating the Peng-Robinson equation of state, Beggs-Brill-based VFP tables, and the adaptive implicit method. Constant-rate and fixed tubing-head-pressure cases were simulated to evaluate the effects of injection and production rates, porosity, and streak permeability on CO_2 migration, gas breakthrough, and storage.

Under constant-rate control, injection-production intensity governed the inter-well pressure difference and gas breakthrough. Higher rates accelerated preferential CO_2 migration, whereas greater porosity improved pressure buffering and storage capacity. Increasing streak permeability reduced injection resistance but promoted earlier gas channeling. Joint interpretation of gas saturation and XMFCO₂ distributions showed that higher injection rates enhanced oil-phase CO_2 enrichment without proportionally expanding the free-gas footprint in the first layer.

Under fixed tubing-head-pressure control, injection and production rates were jointly controlled by VFP characteristics, wellbore pressure losses, and reservoir injectivity and deliverability. Changes in near-well gas mobility and produced gas-liquid ratio affected the injection rate, bottom-hole flowing pressure, and production performance. Across the constant-rate cases, CO_2 storage efficiency ranged from 18.889% to 92.390%. At 430 days under fixed tubing-head-pressure control, cumulative stored CO_2 reached $10{,}745.290 \times 10^3$ sm^3, corresponding to a storage efficiency of 87.992%, with only 12.008% of the injected CO_2 produced.

These results demonstrate that tubing-head pressure constraints, wellbore pressure conversion, reservoir properties, and preferential-flow pathways should be considered jointly to balance flooding performance, CO_2 retention, and gas-channeling risk. Future work will validate and calibrate the model using field pressure, production, fluid-composition, and gas-breakthrough data.

Author contributions: Conceptualization, BD, HM, HZ, JL (Jiaxu Liu) and XR; methodology, BD, HM, JL (Jincang Li) and JL (Jiaxu Liu); software, BD, HM, JL (Jincang Li), KJ and JL (Jiaxu Liu); validation, BD, HM, JL (Jincang Li), KJ, XL and SC; formal analysis, BD, HM and JL (Jincang Li); investigation, BD, HM, JL (Jincang

Li), KJ, XL and TZ; resources, JL (Jincang Li), KJ, TZ, HZ and XR; data curation, BD, HM, JL (Jincang Li), KJ, XL and XO; writing—original draft preparation, BD, HM and JL (Jiaxu Liu); writing—review and editing, BD, HM, JL (Jincang Li), HZ, JL (Jiaxu Liu) and XR; visualization, BD, HM, JL (Jincang Li), KJ, XL, SC and XO; supervision, HZ and XR; project administration, HZ and XR; funding acquisition, HZ and XR. All authors have read and agreed to the published version of the manuscript.

Funding: This work was funded by the National Science and Technology Major Project of China (2025ZD1401106), the General Program of Natural Science Foundation of Hubei Province (2026AFB760), the General Program of National Natural Science Foundation of China (NSFC) (52574028), the Youth Science Fund (Category A) (52525403), and the Xinjiang Uygur Autonomous Region Scientific and Technological Innovation Team Project (2024TSYCTD0018).

Institutional review board statement: Not applicable.

Informed consent statement: Not applicable.

Data availability statement: The data used in this study are available from the corresponding authors upon reasonable request.

Conflict of interest: The authors declare no conflict of interest.

AI use statement: During the preparation of this manuscript, the authors used OpenAI Codex solely for language refinement. No AI tools were used for data analysis, interpretation, or generation of scientific content. All outputs were critically reviewed and edited by the authors. The authors take full responsibility for the integrity and accuracy of the work.

References

1. Metz B, Davidson O, de Coninck HC, et al. IPCC Special Report on Carbon Dioxide Capture and Storage. Cambridge University Press; 2005.
2. Bachu S. CO_2 storage in geological media: Role, means, status and barriers to deployment. Progress in Energy and Combustion Science. 2008; 34(2): 254–273. doi: 10.1016/j.pecs.2007.10.001
3. Godec ML, Kuuskraa VA, DiPietro P. Opportunities for using anthropogenic CO_2 for enhanced oil recovery and CO_2 storage. Energy & Fuels. 2013; 27(8): 4183–4189. doi: 10.1021/ef302040u
4. Núñez-López V, Moskal E. Potential of CO_2-EOR for near-term decarbonization. Frontiers in Climate. 2019; 1: 5. doi: 10.3389/fclim.2019.00005
5. Zhu Y, Wu Z, Ren Y, et al. Unraveling adsorption and pore plugging mechanisms of multi-component shale oil in organic and inorganic nanopores: A molecular dynamics study. Fuel. 2026; 427: 140139. doi: 10.1016/j.fuel.2026.140139
6. Sikanyika EW, Wu Z, Mbarouk MS, et al. Numerical simulation of the oil production performance of different well patterns with water injection. Energies. 2023; 16(1): 91. doi: 10.3390/en16010091
7. Zhu Q, Wu K, Guo S, et al. Pore-scale investigation of CO_2-oil miscible flooding in tight reservoir. Applied Energy. 2024; 368: 123439. doi: 10.1016/j.apenergy.2024.123439
8. Wang Z, Li S, Wei Y, et al. Investigation of oil-based CO_2 foam EOR and carbon mitigation in a 2D visualization physical model: Effects of different injection strategies. Energy. 2024; 313: 133800. doi: 10.1016/j.energy.2024.133800
9. Rao X. The first application of quantum computing algorithm in streamline-based simulation of water-flooding reservoirs. In: Proceedings of the Abu Dhabi International Petroleum Exhibition and Conference; 4–7 November

2024; Abu Dhabi, United Arab Emirates. doi: 10.2118/221850-MS
10. Rao X, He X, Kwak H, et al. A hybrid method combining mimetic finite difference and discontinuous Galerkin for two-phase reservoir flow problems. International Journal for Numerical Methods in Fluids. 2025; 97(4): 484–502. doi: 10.1002/fld.5367
11. Sheng JJ. Enhanced oil recovery in shale reservoirs by gas injection. Journal of Natural Gas Science and Engineering. 2015; 22: 252–259. doi: 10.1016/j.jngse.2014.12.002
12. Song Z, Song Y, Li Y, et al. A critical review of CO_2 enhanced oil recovery in tight oil reservoirs of North America and China. Fuel. 2020; 276: 118006. doi: 10.1016/j.fuel.2020.118006
13. Holm LW, Josendal VA. Mechanisms of oil displacement by carbon dioxide. Journal of Petroleum Technology. 1974; 26(12): 1427–1438. doi: 10.2118/4736-PA
14. Stalkup Jr FI. Miscible Displacement. Society of Petroleum Engineers; 1983.
15. Orr Jr FM. Theory of Gas Injection Processes. Tie-Line Publications; 2007.
16. Kumar N, Augusto Sampaio M, Ojha K, et al. Fundamental aspects, mechanisms and emerging possibilities of CO_2 miscible flooding in enhanced oil recovery: A review. Fuel. 2022; 330: 125633. doi: 10.1016/j.fuel.2022.125633
17. Wang T, Wang L, Meng X, et al. Key parameters and dominant EOR mechanism of CO_2 miscible flooding applied in low-permeability oil reservoirs. Geoenergy Science and Engineering. 2023; 225: 211724. doi: 10.1016/j.geoen.2023.211724
18. Ren J, Xiao W, Pu W, et al. Characterization of CO_2 miscible/immiscible flooding in low-permeability sandstones using NMR and the VOF simulation method. Energy. 2024; 297: 131211. doi: 10.1016/j.energy.2024.131211
19. Song R, Tang Y, Wang Y, et al. Pore-scale numerical simulation of CO_2-oil two-phase flow: A multiple-parameter analysis based on phase-field method. Energies. 2023; 16(1): 82. doi: 10.3390/en16010082
20. Chi J, Ju B, Wang J, et al. A novel numerical simulation of CO_2 immiscible flooding coupled with viscosity and starting pressure gradient modeling in ultra-low permeability reservoir. Frontiers of Earth Science. 2023; 17: 884–898. doi: 10.1007/s11707-023-0085-y
21. Rao X, He X, Xu Y, et al. Numerical simulation of carbon dioxide flooding in fractured reservoirs using generic projection-based embedded discrete fracture model. Physics of Fluids. 2024; 36(10): 106601. doi: 10.1063/5.0225059
22. Rao X, Luo C, He X, et al. An efficient quantum neural network model for prediction of carbon dioxide (CO_2) sequestration in saline aquifers. In: Proceedings of the Abu Dhabi International Petroleum Exhibition and Conference; 4–7 November 2024; Abu Dhabi, United Arab Emirates. doi: 10.2118/222257-MS
23. Peng DY, Robinson DB. A new two-constant equation of state. Industrial & Engineering Chemistry Fundamentals. 1976; 15(1): 59–64. doi: 10.1021/i160057a011
24. Coats KH. An equation of state compositional model. Society of Petroleum Engineers Journal. 1980; 20(5): 363–376. doi: 10.2118/8284-PA
25. Nghiem LX, Fong DK, Aziz K. Compositional modeling with an equation of state. Society of Petroleum Engineers Journal. 1981; 21(6): 687–698. doi: 10.2118/9306-PA
26. Young LC, Stephenson RE. A generalized compositional approach for reservoir simulation. Society of Petroleum Engineers Journal. 1983; 23(5): 727–742. doi: 10.2118/10516-PA
27. Beggs HD, Brill JP. A study of two-phase flow in inclined pipes. Journal of Petroleum Technology. 1973; 25(5): 607–617. doi: 10.2118/4007-PA
28. Hasan AR, Kabir CS, Wang X. Development and application of a wellbore/reservoir simulator for testing oil wells. Society of Petroleum Engineers Formation Evaluation. 1997; 12(3): 182–188. doi: 10.2118/29892-PA
29. da Silva DVA, Jansen JD. A review of coupled dynamic well-reservoir simulation. IFAC-PapersOnLine. 2015; 48(6): 236–241. doi: 10.1016/j.ifacol.2015.08.037
30. Peng L, Han G, Chen Z, et al. Dynamically coupled reservoir and wellbore simulation research in two-phase flow systems: A critical review. Processes. 2022; 10(9): 1778. doi: 10.3390/pr10091778
31. Abdelaal M, Zeidouni M. Coupled wellbore-reservoir modelling to evaluate CO_2 injection rate distribution over thick multilayer storage zones. International Journal of Greenhouse Gas Control. 2023; 129: 103987. doi: 10.1016/j.ijggc.2023.103987
32. Zamani N, Oldenburg CM, Solbakken J, et al. CO_2 flow modeling in a coupled wellbore and aquifer system: Details of pressure, temperature, and dry-out. International Journal of Greenhouse Gas Control. 2024; 132: 104067. doi: 10.1016/j.ijggc.2024.104067
33. Tavagh Mohammadi B, Jahanbani Ghahfarokhi A, Grimstad AA. A review of modeling approaches for CO_2 injection

into depleted gas reservoirs: Coupling transient wellbore and reservoir dynamics. International Journal of Greenhouse Gas Control. 2025; 145: 104406. doi: 10.1016/j.ijggc.2025.104406
34. Koval EJ. A method for predicting the performance of unstable miscible displacement in heterogeneous media. Society of Petroleum Engineers Journal. 1963; 3(2): 145–154. doi: 10.2118/450-PA
35. Luo J, Hou Z, Feng G, et al. Effect of reservoir heterogeneity on CO_2 flooding in tight oil reservoirs. Energies. 2022; 15(9): 3015. doi: 10.3390/en15093015
36. Khan MY, Mandal A. The impact of permeability heterogeneity on water-alternating-gas displacement in highly stratified heterogeneous reservoirs. Journal of Petroleum Exploration and Production Technology. 2022; 12(3): 871–897. doi: 10.1007/s13202-021-01347-3
37. Li J, Cui C, Wu Z, et al. Study on the migration law of CO_2 miscible flooding front and the quantitative identification and characterization of gas channeling. Journal of Petroleum Science and Engineering. 2022; 218: 110970. doi: 10.1016/j.petrol.2022.110970
38. Zhang L, Li C, Zhang Y, et al. CO_2-EOR and storage in a low-permeability oil reservoir: Optimization of CO_2 balanced displacement from lab experiment to numerical simulation. Geoenergy Science and Engineering. 2024; 243: 213325. doi: 10.1016/j.geoen.2024.213325
39. Li Z, Xu T, Tian H, et al. The impacts of reservoir heterogeneities on the CO_2-enhanced oil recovery process—A case study of Daqingzijing Block in Jilin Oilfield, China. Energies. 2024; 17(23): 6128. doi: 10.3390/en17236128
40. Zhang YQ, Yang SL, Bi LF, et al. A technical review of CO_2 flooding sweep-characteristics research advance and sweep-extend technology. Petroleum Science. 2025; 22(1): 255–276. doi: 10.1016/j.petsci.2024.09.005